



Science Arts & Métiers (SAM)

is an open access repository that collects the work of Arts et Métiers Institute of Technology researchers and makes it freely available over the web where possible.

This is an author-deposited version published in: <https://sam.ensam.eu>
Handle ID: <http://hdl.handle.net/10985/24861>

To cite this version :

Margaux HAURAT, Yannick ANGUY, Cécile GABORIEAU, Guillaume AUBERT, Cyril AYMONIER, Michel DUMON - High-pressure drop rates in solid-state batch one-step scCO₂ foaming of acrylic polymers: A way to stabilize the structure of micro-nano foams - Chemical Engineering Science - Vol. 281, p.119099 - 2023

Any correspondence concerning this service should be sent to the repository

Administrator : scienceouverte@ensam.eu



High-pressure drop rates in solid-state batch one-step scCO₂ foaming of acrylic polymers: a way to stabilize the structure of micro-nano foams

Margaux Haurat¹, Yannick Anguy^{2*}, Cécile Gaborieau², Guillaume Aubert³, Cyril Aymonier³, Michel Dumon^{*1}

¹ Université de Bordeaux, UMR CNRS 5629, Bordeaux INP, LCPO, UMR 5629, ENSCBP 16 avenue Pey Berland, F-33600 Pessac, France

² Université de Bordeaux, UMR CNRS 5295 I2M, F-33405, Talence, France

³ Université de Bordeaux, UMR CNRS 5026, Bordeaux INP, ICMCB, UMR 5026, F-33600 Pessac, France

*Contact authors to whom correspondence should be addressed: yannick.anguy@u-bordeaux.fr and michel.dumon@u-bordeaux.fr

Abstract

One-step solid-state batch scCO₂ foaming is used with the target of achieving acrylic polymer micro-nano foams. Foaming is triggered by an average pressure drop (APDR), covering two decades, from 0.3 to 30 MPa.s⁻¹. This study principally addresses the combined beneficial effects of block copolymer addition (BCP, here denoted as MAM) and high APDR. Numerous subtle kinetic parameters actually interplay and compete in the production of the final foams. In particular, the material effective temperature, the effective glass transition temperature of the plasticized system and the instantaneous PDR are physical quantities each having their own kinetics during foaming. The resulting foam morphologies are quantified by SEM microscopy and image analysis. A high APDR and the presence of BCP are shown to play a key role in the final structure of the foams. Over the scrutinized range of saturation temperature (40 °C to 60 °C *i.e.* rather 'low' temperatures in the CO₂ supercritical state), the APDR is the main factor for significantly reducing cell size and increasing nuclei density in foams from neat PMMA. In the block copolymer approach, increasing the APDR is of secondary importance as the targeted reduction of the porosity dimensions and augmentation of nuclei density are mostly the consequence of MAM presence. In this latter case, increasing the APDR still promotes the 'efficiency' of the BCP nucleants. A real efficient nucleation activity of MAM additive is observed at a very high APDR (30 MPa.s⁻¹), leading to monomodal homogeneous distribution of tiny pores in nearly nanosized foams. At lower APDR, an interesting reproducible double porosity (foams containing intra-wall and inter-cell pores) is detected in PMMA/MAM systems. In such double porosity foams, benefits from the Knudsen effect achieved within well expanded local domains (showing micron-sized pores) may remain meaningful thanks to a locally poorly expanded nanoporous thick solid skeleton encapsulating these local domains. Thereby, the radiative thermal conduction can be minimized and does not override the conductive component at the sample scale. This work provides further insight on acrylic polymer BCP foams influenced by different kinetics.

38

39 **Keywords:** supercritical carbon dioxide; micro-nano foams; one-step batch foaming; high-pressure
40 drop rate; acrylic polymers; quantitative structural analysis; foaming process; thermal insulation

41 **1. Introduction**

42 In recent years, polymer foams, and especially micro-nano foams obtained by a blowing (or foaming)
43 agent, have raised the interest of industrials and academics due to their expected unusual
44 combination of properties. Indeed, reducing the foam porosity dimensions from micro to nano range
45 can lead to improved mechanical and thermal insulation properties (e.g. due to the Knudsen effect
46 for the latter) [1],[2], or even filtration properties. However, when a blowing agent is used, the
47 desired porosity size reduction is not easy to reach and requires optimization of the foaming process
48 conditions (e.g. saturation pressure, temperature, and time, pressure drop rate) for each foaming
49 agent – material – process combination.

50 The foaming agent is either chemical or physical. Chemical foaming requires use of a chemical
51 blowing agent to generate a gas by thermal decomposition or by chemical reaction [3]. On the
52 contrary, a physical blowing agent (e.g. an inert gas) is directly injected in the process [4],[5],[6]. In
53 both cases, a thermodynamic instability is required to induce a phase separation between the gas
54 and the material. At that point, foaming is initiated and the nucleation, growth and coalescence steps
55 ensue. Depending on the foaming conditions, all three steps may, or not, partially overlap over time.
56 In order to propose a more environmental responsible alternative than chemical foaming, carbon
57 dioxide (CO₂) is selected as the physical blowing agent. This non-toxic and low-cost blowing agent
58 enters the supercritical state (scCO₂) in rather easy conditions, with a critical point at $P_C = 7.38 \text{ MPa}$
59 and $T_C = 31 \text{ }^\circ\text{C}$. In these specific conditions, CO₂ offers a combination of liquid and gaseous
60 properties *i.e.* good solubility and diffusivity in polymers (in comparison with other physical blowing
61 agents, e.g. nitrogen) [7]. The supercritical specificities are thus favorable for polymer saturation and
62 to some extent for polymer foaming (as pressure is released, the blowing agent leaves rapidly the
63 supercritical state).

64 Considering the high CO₂-philicity and the ability to foam with reduced porosity dimensions of acrylic
65 polymers, they are good candidates for scCO₂-assisted saturation/foaming [8],[9]. Both neat
66 poly(methyl methacrylate) (PMMA) and blends of PMMA + MAM – the so-called MAM is a triblock
67 copolymer PMMA-PBA-PMMA (where PBA is poly(butyl acrylate)) – have been largely studied in the
68 literature and were selected for this study. In a 90/10 PMMA/MAM weight ratio solid precursor
69 blend, MAM structures are typically nano micellar-like objects dispersed in the PMMA matrix. Due to
70 the higher CO₂-philicity of the soft PBA block, the micellar objects concentrate the CO₂ and act as
71 CO₂-reservoirs during saturation and foaming. In the foaming process, the micellar objects are

72 deemed to act as effective nucleation sites (as other additives [10]) and to improve PMMA foaming
73 (foam homogeneity and cell size reduction) [6],[11],[12],[13].

74 Acrylic polymers can be saturated and foamed using various processes assisted with scCO₂; one can
75 quote extrusion [4],[14], injection [5],[15] and batch foaming (either one-step or two-step)
76 [6],[11],[16]. So far, batch foaming (or autoclave foaming) is preferred over the other processes to
77 produce foams with small porosities [12],[16]. Indeed, contrary to other processes, all batch
78 saturation conditions (*i.e.* saturation pressure, temperature and time), are independently controlled
79 [8]. In view of solid-state one-step batch foaming with reduced porosity dimensions, the roles of the
80 saturation pressure and temperature upon acrylic polymers-foaming are well known [17],[18]. On the
81 one hand, saturation pressure (P^{sat}) has to be maximized to improve the sample saturation by
82 increasing the CO₂-solubility [9]. On the other hand, saturation temperature (T^{sat}) has to be
83 minimized to optimize the saturation step, while complying with the supercritical state, which also
84 contributes to optimize the saturation step due to an advantageous combination of liquid and
85 gaseous properties. The relation between T^{sat} and the speed at which the foam vitrifies (or
86 stabilizes) is a complex issue, certainly overlooked in the literature. Indeed, as foaming is triggered
87 e.g. by an adiabatic pressure *quench*, the effective temperature (T^{ef}) of the plasticized system
88 {polymer + CO₂} is lower than T^{sat} and generally unknown. The vitrification speed is therefore
89 determined, among others, by the interplay between *i)* the evolution of T^{ef} towards room
90 temperature and *ii)* the rising kinetics of the effective glass transition temperature (T_g^{ef}). Once the
91 sample is vitrified ($T_g^{ef} > T^{ef}$), cell growth and coalescence are stopped and one can expect to
92 produce a foam with small cell dimensions.

93 At the beginning of foaming, another important parameter acts on the foam structure: the pressure
94 drop rate (PDR). The pressure drop rate is typically defined as $\Delta P/\Delta t$, where $\Delta P = p^{sat} - p^{ambient}$
95 and Δt is the time to return to ambient pressure upon pressure release [19]. Several studies have
96 shown that increasing the pressure drop rate is a relevant way to minimize foam cell size thereby
97 improving the mechanical and thermal properties [19],[20],[21]. This trend has been observed using
98 adapted devices (e.g. PP batch-foaming fitted with a window linked to a camera [22]) allowing
99 observation of the foaming process from the early stages of cell growth. A PDR increase induces an
100 increase of the nuclei formation rate [23]. At a certain stage, nucleation and growth may compete.
101 More precisely, when cell nucleation and growth overlap, the later penalizes the former. When the
102 PDR is increased, the nucleation rate is favored while growth is limited. Increasing the PDR also
103 prevents coalescence by increasing the speed at which the effective glass temperature of the
104 plasticized system {polymer + CO₂} (T_g^{ef}) is overcome (*i.e.* $T^{ef} < T_g^{ef}$) [23],[24]. So, because of its

105 action upon the different foaming steps, the PDR has an influence upon both cell size and cell density
106 [24],[25],[26],[27].

107 In batch foaming, a *classical* PDR value may be considered as $0.5 \text{ MPa}\cdot\text{s}^{-1}$ [11]; other PDR values have
108 been studied ($30 \text{ MPa}\cdot\text{s}^{-1}$ [19]; $8.3 \text{ MPa}\cdot\text{s}^{-1}$ [24]; $0.4 \text{ MPa}\cdot\text{s}^{-1}$ [28]) by using vessels with a smaller
109 capacity and/or by increasing the outlet pipe diameter to facilitate gas evacuation during foaming.
110 Experimentally, the number of nucleated bubbles per unit volume of unfoamed material (N_0) has
111 been shown to depend linearly upon pressure drop rate in a bi logarithmic scale [24]. A classical PDR
112 ($\sim 0.5 \text{ MPa}\cdot\text{s}^{-1}$) is generally not sufficient to reach a very small pore size as it does not induce a
113 sufficient number of nuclei or do not freeze the structure by a rapid enough thermal quench
114 (consecutive to pressure quench). Simulations of PDR were carried out at an extremely high PDR
115 ($250 \text{ MPa}\cdot\text{s}^{-1}$) [20],[26]. As a matter of fact, both theoretical and experimental studies show that a
116 PDR increment can increase the cell number density by 1 or 2 decades while cell size decreases by a
117 moderate factor of 2 or 3. Furthermore, most of the systems studied in the literature are probably in
118 a molten state (flowing state), and do not undergo a solid-state (non-flowing) foaming. Thus we may
119 expect a greater influence of the PDR value when the system is solid (solid-state CO_2 foaming).

120 No work actually states clearly if the mere fact to increase the pressure release rate can increase the
121 cell density ($\text{cells}\cdot\text{cm}^{-3}$) up to $10^{15} \text{ cell}\cdot\text{cm}^{-3}$, reduce cell size in the nanometer range and
122 simultaneously lower the overall material density (ρ_f) near or below $0.2 \text{ g}\cdot\text{cm}^{-3}$. However, in a one-
123 step solid-state batch foaming, appropriate combinations of factors (high PDR, low saturation
124 temperature and introduction of nucleating nano particles) may be beneficial. Such combinations are
125 investigated in this work for neat PMMA and for PMMA/10 wt% MAM blend foams. PMMA and
126 PMMA/10 wt% MAM are CO_2 -saturated at temperatures ($40 \text{ }^\circ\text{C}$ and $60 \text{ }^\circ\text{C}$) and saturation pressures
127 (20 MPa and 30 MPa) complying with the supercritical state before being foamed (one-step solid-
128 state foaming) over a broad PDR range (from $0.3 \text{ MPa}\cdot\text{s}^{-1}$ to $30 \text{ MPa}\cdot\text{s}^{-1}$). Porous structures are
129 investigated through a quantitative analysis of SEM images at different scales.

130

131 **2. Materials and Methods**

132 **2.1 Materials**

133 Neat poly(methyl methacrylate) (PMMA commercialized as V825T 101 Clear PMMA by Arkema)
134 pellets and neat MAM (M53 grade commercialized by Arkema) triblock copolymer (poly(methyl
135 methacrylate)-co-poly(butyl acrylate)-co-poly(methyl methacrylate)) pellets were supplied by
136 Arkema (Lacq, France). The characteristics of these materials are well documented in literature
137 [12],[18],[29].

138 **2.2 Unfoamed blend compounding**

139 To produce PMMA/10 wt% MAM blend, neat PMMA and MAM pellets were first dried at 80 °C for
140 4 h in an oven. Then, the blend was compounded by CANOE (Pau, France) using a corotative twin-
141 screw extruder (Labtech, $\phi = 26 \text{ mm}$, $L/D = 40$) with a temperature profile ranging from 250 °C to
142 230 °C at a screw speed of 300 rpm. At the end of the extruder line, the blend was pelletized with a
143 continuous cutting machine.

144 Neat PMMA and PMMA/10 wt% MAM pellets were dried again at 80 °C for 4 h in an oven. Then,
145 transparent tensile test bars (ISO 180/U $80 \times 10 \times 4 \text{ mm}^3$) of neat PMMA and PMMA/10 wt% MAM
146 were injected with a classical injection-molding device (ENGEL ES 200-45 HL-V). The acrylic polymer
147 and blend were injected at 230 °C at a screw speed of 300 rpm in a mold heated at 90 °C. All injected
148 bulk bars were perfectly transparent.

149 **2.3 One-step batch foaming**

150 PMMA and PMMA/10 wt% MAM were foamed through scCO₂-assisted one-step batch process at
151 LCPO and ICMCB laboratories (Bordeaux, France). Varying the PDR over a wide range of values
152 typically requires use of vessels of different capacities and/or outlet pipe diameter [19], [24], [28]. In
153 this study, two vessels were used to vary the PDR by two order of magnitude (Table 1). These two
154 vessels were especially necessary to be able to work with sufficiently large samples; and the bigger-
155 sized vessel could in no way allow reaching 30 MPa.s⁻¹.

156 The samples foamed at « low PDR » (0.3 MPa.s⁻¹ and 0.5 MPa.s⁻¹) were produced in a high-pressure
157 vessel provided by TOP Industrie (Vaux-le-Pénil, France). The vessel was filled with CO₂ at the desired
158 pressure with a syringe pump Teledyne ISCO model 260 (Lincoln, USA). Because the outlet pipe
159 diameter was fixed, the saturation pressure was set to 20 MPa or 30 MPa to enforce the target PDRs
160 of 0.3 and 0.5 MPa.s⁻¹ (values in the range of low PDR). The saturation temperature (40 °C or 60 °C)
161 was controlled with a heating collar. The CO₂ uptake (wt%) was measured in situ using a FTIR (Fourier
162 Transform Infrared) microscope combined to a CO₂ high-pressure cell [9]; scCO₂ uptake was found to
163 the same at 20 MPa and 30 MPa (the samples are already fully saturated at 20 MPa at both
164 temperatures) [9]. Therefore, a saturation pressure spread of 10 MPa (20 vs. 30 MPa) had no impact
165 upon the final foam structures. After saturation (during 24 h to ensure full saturation of the samples),
166 the pressure was released with an on/off discharge valve model 910.10.00 provided by TOP Industrie
167 (Vaux-le-Pénil, France).

168 Samples foamed at higher PDR (4 MPa.s⁻¹ and 30 MPa.s⁻¹) were produced in a smaller-sized vessel
169 (0.057 L) provided by Swagelok (Lyon, France). In this vessel, the PDR could be varied by adapting the
170 geometry of the vessel (outlet pipe diameter; Table 1). After saturation (24 h), the pressure was
171 released with an on/off discharge valve model SS-AFSS12 provided by Swagelok (Lyon, France).

172 **Table 1.** Batch set-up dimensions versus PDR

PDR (MPa.s ⁻¹)	Vessel capacity (cm ³)	Outlet pipe internal diameter (cm)
0.3	300	0.2
0.5	300	0.2
4	57	2.36
30	57	13.51

173

174 2.4 Characterization techniques

175 i. Water pycnometer

176 Unfoamed materials density (ρ_s) and foams density (ρ_f) were determined with a water pycnometer
 177 following the water displacement method, based on Archimedes' principle. Three measurements
 178 were performed for each sample.

179 ii. Electron microscopy observations and image analysis

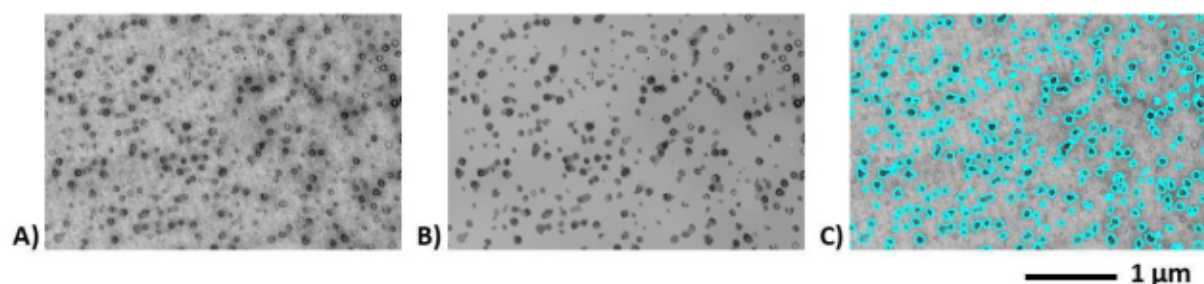
180 • PMMA/10 wt% MAM dense precursor blend: TEM observations

181 The structure of the solid PMMA/10 wt% MAM blend precursor was observed through TEM. Before
 182 observation, the solid blend was cut into a cryo-ultramicrotome LEICA EM UC7-FC7 (Wetzlar,
 183 Germany) at -75 °C with a diamond knife at the Bordeaux Imaging Center (BIC, Bordeaux, France).
 184 The thin cuts (80 – 100 nm thick) were collected on copper grids before being contrasted with an
 185 aqueous solution containing 2 wt% phosphotungstic acid (PTA) + 2 wt% benzyl alcohol at ambient
 186 temperature. As reported in the literature, PTA preferentially colors at ambient temperature the
 187 CO₂-philic PBA soft block (in black or dark grey on TEM images) over the PMMA more rigid block
 188 (white or light grey on TEM images) [6],[11]. Benzyl alcohol acts as a dyeing assistant and helps PTA
 189 coloration of PBA. TEM observations were performed at 80 kV at magnifications ranging from
 190 X15 000 to X200 000 (Figure 1.A). The exhibited nanostructures can be qualified as micellar objects or
 191 micelle-like objects.

192 • Image analysis of TEM micrographs

193 TEM images captured at several magnifications were analyzed in order to quantify the micellar
 194 objects and determine automatically their characteristics. To further improve the level of contrast
 195 permitted by staining (Figure 1.A) and facilitate the subsequent segmentation of the micellar objects
 196 (Figure 1.C), we adopted a multiscale (multiresolution) description of electronic images (thereafter
 197 electronic images are denoted by $u(\mathbf{x})$, where u is the grey level intensity function at every pixel $\mathbf{x} =$
 198 (x_1, x_2)). Descriptions that depend on scale (or resolution) may be computed in several ways. We
 199 retained the so-called *scale-space filtering* [30],[31]. In this approach, the original image $u(\mathbf{x})$ (Figure
 200 1.A) is embedded in a family of images $u(\mathbf{x}, t)$ at coarser resolutions (larger scale levels) *cf* e.g. Figure
 201 1.B. Such family of images $u(\mathbf{x}, t)$ is obtained by filtering $u(\mathbf{x})$ over increasing scales whose size is
 202 parametrized by the increasing time t of a diffusion equation [32]. The resulting family of images
 203 $u(\mathbf{x}, t)$ produced by varying continuously the scale-space parameter t is called the scale-space image.

204 Because information content decreases towards higher levels (at coarser resolutions), edges or
 205 boundaries (the zero-crossings of the Laplacian of the image) are moved when sweeping out the
 206 scale-space image. In this sense, we can say that the material is virtually reconstructed as illustrated
 207 in Figure 1.B. With this multiscale (multiresolution) description, we could detect more readily image
 208 features at different resolutions (e.g. Figure 1.B). In this approach, the key point is that images have
 209 by nature a hierarchical organization composed of a small number of levels or scales [33]. There is a
 210 natural range of resolutions, in other words intervals of the scale-space parameter t , corresponding
 211 to each of these *semantic* levels of description, where the interphases and/or interfaces of interest
 212 are better perceived and even reconstructed (Figure 1.B). As illustrated in Figure 1.B, the
 213 reconstructed image tends to a piecewise constant solution representing a simplified image with
 214 sharper boundaries, permitting to easily segment interphases e.g. by direct thresholding without
 215 recourse to any complex treatment of image analysis. To achieve this, we followed the route paved
 216 by Perona and Malik [34]. We relied on a nonlinear scale space, where blurring is locally adaptive to
 217 image data: the diffusion process (blurring) mainly takes place in *flat* regions (PMMA matrix) where
 218 the magnitude of the gradient $\left(\nabla(\cdot) = \left(\frac{\partial(\cdot)}{\partial x_1}, \frac{\partial(\cdot)}{\partial x_2}\right)\right)$ of the grey level intensity $\|\nabla u\|$ is low. On the
 219 other hand, blurring does not affect region boundaries (micellar object boundaries), where $\|\nabla u\|$ is
 220 larger. Furthermore, in the neighborhood of marked discontinuities (boundaries), where $\|\nabla u\|$ is
 221 high across the level curve of the intensity u , the diffusion process is running locally backwards,
 222 normal to the isoline of u *i.e.* normal to the boundary, which is thereby steepened (contrast
 223 enhancement; Figure 1.B).

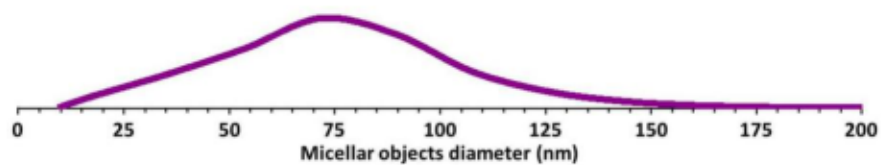


224
 225 **Figure 1.** Illustration of the segmentation of micellar objects. **A)** Local close up in a TEM micrograph (X20 000)
 226 showing dispersed micellar objects formed by MAM tri-block copolymers in a 90/10 PMMA/MAM solid blend
 227 precursor. **B)** Enhanced image after applying to Figure 1.A a nonlinear directional diffusive filter. In this filtering
 228 procedure, Gaussian blurring applies selectively to flat regions, which are dissipated, while the boundaries and
 229 the contrast of the nanostructures of interest are clearly enhanced. **C)** Binarized (0 -1) counterpart of the grey
 230 level image in Figure 1.B. In this display, the contours of the segmented nanostructures (labeled with a 1 value)
 231 are displayed in cyan, superimposed upon the original image (Figure 1.A) rather than leaving in transparency
 232 the 0-valued background matrix.

233 Before segmentation, the filtered image $u(\mathbf{x}, t)$ was, when necessary, corrected for shading (uneven
 234 background matrix). Touching/overlapping micellar objects were automatically separated before size

235 and shape measurements. To do so, we assumed, as others e.g. Canseco et al. [35], a systematic
 236 region growing approach [36]. After disconnection of overlapping objects, the binary image (e.g.
 237 Figure 1.C) was perfectly suited to the automatic measurement of the object size statistical
 238 distribution (Figure 2). The effective diameter D of every micellar object was derived from the object
 239 perimeter P measured by integrating for all affine lines in the plane the Euler-Poincaré characteristic
 240 of the intersection of the line with the object [37].

241 The rather large distribution of the micellar objects diameter (Figure 2) suggests that the system is
 242 not at equilibrium (a liquid micellar system would show a mono modal distribution). The non-
 243 equilibrium state comes from several reasons: *i*) the macromolecular nature and chain polydispersity
 244 of MAM, *ii*) the high viscosity and temperature quenching of the blend during the extrusion stage,
 245 where the blend is sheared and cooled at the end of the die.



246

247 **Figure 2.** Nanostructure size distribution automatically determined from segmented objects (Figure 1.C). In this
 248 display, the finite size interval bins of the original discrete frequency histogram of the object diameters are
 249 schematically represented as a continuous distribution of the object percentile as a function of cell size. The
 250 vertical full scale is set to the highest nanostructure percentile of the original frequency histogram.

251 Some of the characteristics derived from the nanostructure size distribution of the 10 wt% MAM
 252 solid precursor (Figure 2) are listed in Table 2, namely the nanostructure number density N_s
 253 (objects.cm⁻³), the nanostructure average diameter \bar{D}_s and the aggregation number $N_{aggregation}$
 254 (number of copolymer molecules per nanostructure). Assuming that all the copolymer lies inside the
 255 micellar objects, an upper bound of the aggregation number was estimated as:

$$256 \quad N_{aggregation} = \frac{w N_a \rho_s}{M_n N_s} \quad Eq. 1$$

257 where w is the amount of copolymer (wt%) and $N_a = 6.02 \cdot 10^{23} \text{ mol}^{-1}$ the Avogadro's number, M_n
 258 number average molar mass.

259 **Table 2.** Characteristics of PMMA/10 wt% MAM solid precursors.

Solid sample ID	Nanostructure density N_s (objects.cm ⁻³)	Nanostructure average diameter \bar{D}_s (nm)	Density of the solid blend ρ_s (g.cm ⁻³)	Predicted aggregation number $N_{aggregation}$
PMMA/10 wt% MAM	$2.4 \cdot 10^{14} \pm 0.2 \cdot 10^{14}$	68 ± 8	1.19 ± 0.07	3700

260 Compared to the literature, the micellar objects average diameter is consistent with previous
261 determinations. Nevertheless, the number density of $2.4 \cdot 10^{14}$ objects.cm⁻³ seems an insufficient
262 nucleating density to provide true nano foams (requiring an order of magnitude of 10^{15} to
263 10^{16} objects.cm⁻³ [38]).

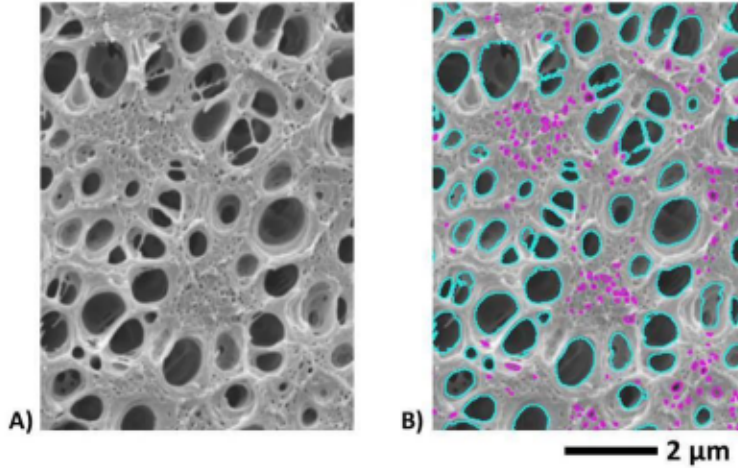
264 • PMMA and PMMA/10 wt% MAM foams: SEM observation

265 PMMA and PMMA/10 wt% MAM foam structures were observed on micrographs acquired with an
266 environmental scanning electron microscope (E-SEM), a Quanta FEG 250 from FEI/ThermoFisher.
267 Before observation, the foamed samples were frozen in liquid nitrogen, fractured (perpendicularly to
268 the height) and sputter-coated with a thin layer of gold. All samples were imaged at low acceleration
269 voltage (< 5 keV) and current (a few pA to a few tens of pA) (not to damage the foam structure with
270 the primary electron beam). Images were formed by collecting the secondary electron (SE) emission.
271 In this situation, contrast is said topographical and is made of three contributions: the inclination
272 contrast, the shading contrast and the ridge contrast. Each sample was imaged at several
273 magnifications (from X100 to X100 000). Figure 3.A illustrates over a local area the structure of a
274 foam sample produced from the 90/10 PMMA/MAM blend at a saturation temperature of 60 °C, and
275 a pressure drop rate of 0.3 MPa.s⁻¹.

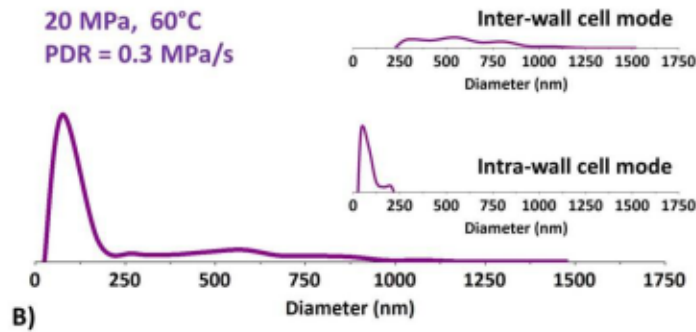
276 • Image analysis of SEM image

277 In micrographs formed in secondary electron mode, both shading and ridge contrasts promote
278 darker foam cells than the polymeric background solid lattice. Yet, dependence of the secondary
279 emission upon the incident angle of the primary electron beam (inclination contrast) may work
280 locally *the other way around*, depending on the local geometry of the sample. Thus, there is again a
281 need to further increase contrast in order to develop a sound automatic method for the
282 determination of the cell size distribution. We took again advantage of the nonlinear directional
283 diffusive filter described earlier to reach a suitable level of (enhanced) contrast. After this contrast
284 augmentation, the segmentation of smooth and darker foam cells standing out from a brighter solid
285 lattice could be accomplished via a simple threshold. The object sets segmented thereby, like the one
286 illustrated in Figure 3.B, were suited for the automatic determination of the object diameter
287 statistical distribution (Figure 4), the diameter of every object being derived from measurement of its
288 perimeter.

289



290
 291 **Figure 3. A)** Cellular structure produced from a PMMA/10 wt% MAM blend saturated with $scCO_2$ at 60 °C and
 292 then foamed in one-step batch-foaming with a pressure release rate of $0.3 \text{ MPa}\cdot\text{s}^{-1}$. **B)** The segmented object set
 293 (cell set) includes inter skeletal pores (in cyan) and intra skeletal pores (in magenta).



294
 295 **Figure 4.** Cell size distribution of the foam sample locally illustrated in Figure 3. The vertical full scale is set to
 296 the highest cell % of the frequency histogram. The foam sample shows two scales of porosity (Figure 3). The
 297 intra- and inter-wall cell size modes of the global (bimodal) size distribution (lower curve) were further specified
 298 by filtering the segmented object set (cell set). Filtering consisted in removing those objects from an object set
 299 whose filter size attribute (e.g. object diameter or area) fell outside a specified range. The chosen object size
 300 attribute threshold value was that one which partitioned unequivocally the cell set in two classes of porosity:
 301 small-sized intra-wall cells (in magenta) versus much larger inter-wall cells (in cyan) (Figure 3).

302 Several important characteristics were derived from the cell size distributions including the cell
 303 number density (N_{cell} , $\text{cell}\cdot\text{cm}^{-3}$), the cell nucleation density (N_0 , $\text{nuclei}\cdot\text{cm}^{-3}$) and the mean cell size
 304 (\bar{D}_{cell}). The cell number density in the porous material (N_{cell}) was calculated using Equation (2).

305
$$N_{cell} = \left(\frac{m}{A}\right)^{3/2} \quad \text{Eq. 2}$$

306 where m is the number of cells segmented in an image (collection of images) and A is the area of the
 307 digital image (collection of digital images) in cm^2 .

308 The cell nucleation density in the foamed material (N_0) represents the number of pores formed per
 309 cubic centimeter of the unfoamed dense blend precursor making implicitly the hypothesis that there
 310 is no coalescence during the stabilization of the foam structure. N_0 was calculated using Equation (3).

311
$$N_0 = N_{cell} \times \frac{\rho_s}{\rho_f} \quad Eq.3$$

312 N_0 can be paralleled to the micellar objects density (N_s) measured in the dense blend precursor.
313 Those values should be ideally as close as possible.

314 SEM images at different scales and their quantitative analysis revealed two scales of pores in several
315 of the foams produced from the 90/10 PMMA/MAM blend *cf* e.g. Figure 3 namely, inter-skeletal
316 micropores (voids separated by cell walls as defined by Kaneko et al. in a general review on solid
317 porous materials [39]) and intra-skeletal much smaller nanopores, located inside the cell walls. In this
318 instance three average diameters were calculated: \bar{D}_{cell} the global mean cell diameter,
319 $\bar{D}_{inter-wall\ cell}$ the inter skeletal pore mean diameter and $\bar{D}_{intra-wall\ cell}$ the intra skeletal pore
320 mean diameter. When intra skeletal pores are present, \bar{D}_{cell} contains information (weighted
321 average) from $\bar{D}_{inter-wall\ cell}$ and $\bar{D}_{intra-wall\ cell}$; while $\bar{D}_{cell} \equiv \bar{D}_{inter-wall\ cell}$ when there is no
322 intra skeletal pores. The size distributions (including the inter wall and intra wall cell modes in case of
323 bimodal distribution *cf* e.g. Figure 4) of all studied foam samples are provided and discussed in the
324 next section.

325

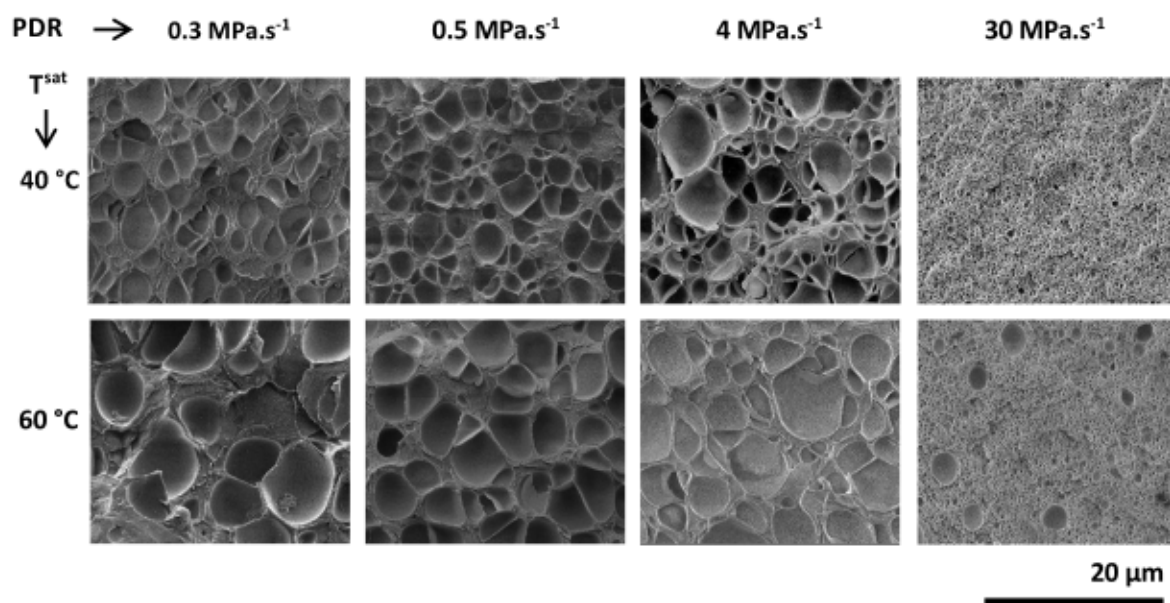
326 **3. Results and discussion**

327 **3.1 Porous structures after one-step batch foaming (SEM Imaging)**

328 This section (3.1) describes qualitatively the different morphologies observed on SEM micrographs
329 and outlines general trends. The next section (3.2) deals with the quantification of the structural
330 information contained in the SEM micrographs.

331 **3.1.1 PMMA foam structures**

332 Neat PMMA samples were foamed at PDR ranging from 0.3 MPa.s⁻¹ to 30 MPa.s⁻¹. The influence of
333 the saturation temperature and the PDR on the structure of the final PMMA foams is illustrated in
334 Figure 5.



335

336 **Figure 5.** SEM images of neat PMMA saturated at either 40 °C or 60 °C ($P^{sat} = 20$ MPa or 30 MPa) at a PDR
 337 ranging from 0.3 MPa.s⁻¹ to 30 MPa.s⁻¹ (in a one-step batch foaming process)

338

339 At a fixed saturation temperature (either 40 °C or 60 °C), PMMA foamed at low to moderate PDR (*i.e.*
 340 between 0.3 MPa.s⁻¹ and 4 MPa.s⁻¹) are comparable. In other words, at a given temperature, the
 341 foam cell size is not significantly influenced by the PDR value (Figure 5). Although the foam cells of
 342 the samples scCO₂-saturated at 40 °C appear a little smaller than those of the samples saturated at
 343 60 °C, the cell dimension remains in the same order of magnitude at low to moderate PDR.

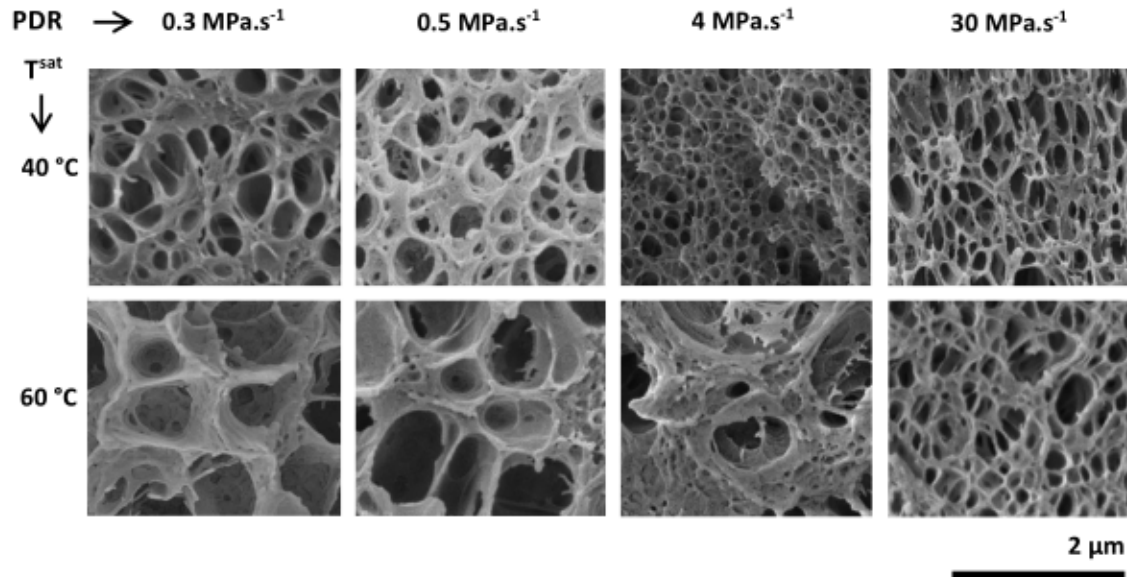
344 Only a high PDR of 30 MPa.s⁻¹ induces a true change towards much smaller cells. Moreover, the
 345 sample foamed at 30 MPa.s⁻¹ after a saturation at 60 °C contains two types of porosities, while the
 346 sample saturated at 40 °C is monomodal (only small pores).

347 As a first global summary for PMMA foams, the cell dimension is mainly governed by the saturation
 348 temperature at low to moderate PDR, while cell dimension is principally governed by PDR at
 349 30 MPa.s⁻¹.

350

351 3.1.2 PMMA/10 wt% MAM foam structures

352 PMMA/10 wt% MAM blend samples were foamed in the same conditions as for neat PMMA (Figure
 353 6). As observed in the case of PMMA, saturation temperature and PDR are competing to determine
 354 the PMMA/10 wt% MAM final foam structure.



355

356 **Figure 6.** SEM images of PMMA/10 wt% MAM blend foamed after saturation at 40 °C and 60 °C ($P^{sat} = 20$ MPa
 357 or 30 MPa) using a PDR ranging from 0.3 MPa.s⁻¹ to 30 MPa.s⁻¹ (in one-step batch foaming process).

358

359 At fixed temperature, PMMA/10 wt% MAM samples foamed at low PDR (0.3 to 0.5 MPa.s⁻¹) are not
 360 significantly affected by the PDR value (Figure 6). But, over that PDR range, the scCO₂ saturation
 361 temperature plays a more important role upon the inter-wall cell size: the lower the saturation
 362 temperature is, the smaller is the inter-wall cell size.

363 At the moderate PDR of 4 MPa.s⁻¹, both the saturation temperature and the PDR impact cell size. At
 364 40 °C, the 4 MPa.s⁻¹ PDR leads to a much smaller cell size than at lower PDR, while at 60 °C, the inter-
 365 wall cell size is still comparable to that observed at lower PDR.

366 Samples foamed at the highest PDR (30 MPa.s⁻¹) contain small cells of the same size independently of
 367 the saturation temperature, which no longer impacts the final foam structure.

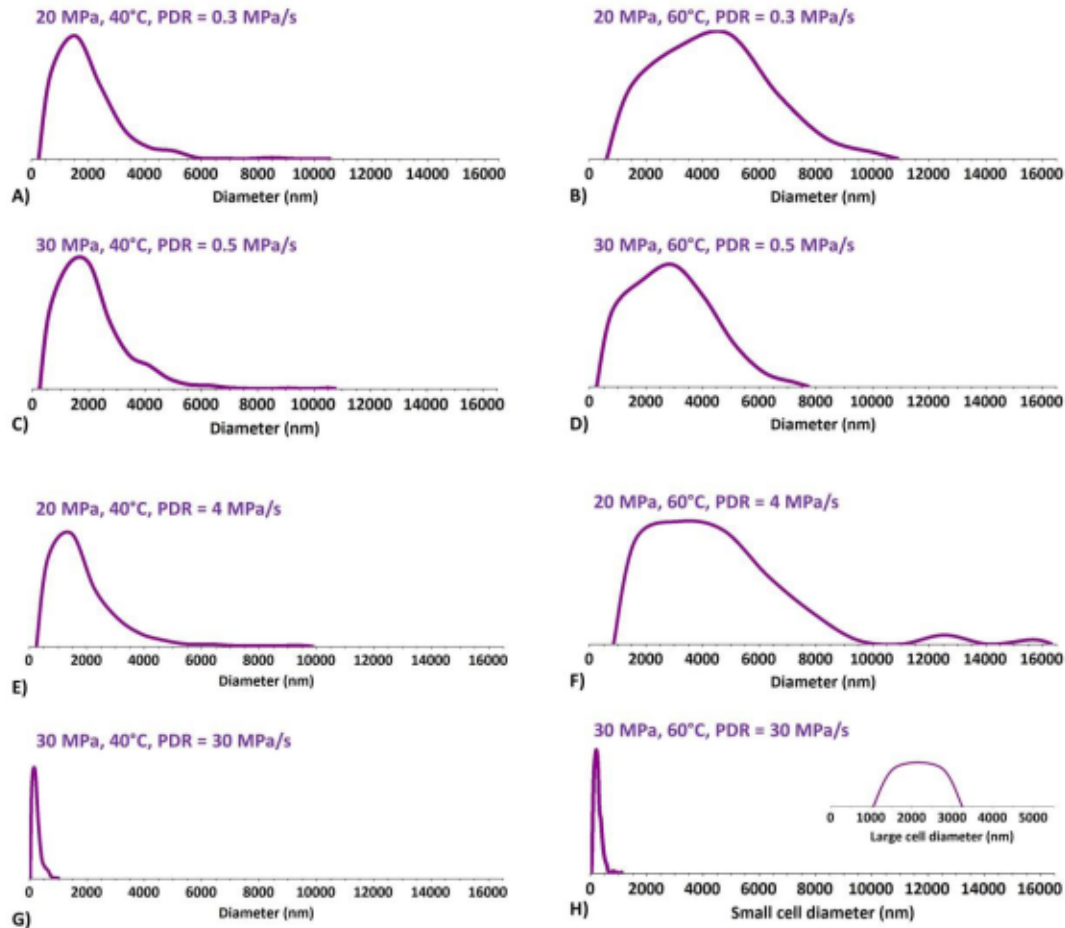
368 Whatever the thermodynamic conditions are (P^{sat} , T^{sat} , t^{sat} , PDR), the addition of MAM in PMMA
 369 systematically induces smaller porosity dimensions than in neat PMMA foams (note that Figure 6 is
 370 shown at a scale ten times smaller than in Figure 5). This trend of cell size reduction, already
 371 reported in the literature, can be explained in terms of CO₂ local concentration, heterogeneous
 372 nucleation and increased cell density [7],[8],[9],[10],[11].

373 As a first conclusion, in a one-step solid-state foaming, if the material formulation always influences
 374 the foam structure, a high PDR acts as a supplementary beneficial variable to efficiently achieve the
 375 targeted cell size reduction as observed by SEM imaging.

376

3.2 Structural quantification by image analysis

377 This section presents the structural quantification of PMMA and PMMA/10 wt% MAM foams by
 378 image analysis. For each foam sample, several SEM images captured at various magnifications were
 379 automatically segmented according to the procedure presented in Section 2.4 in order to determine
 380 a representative cell size statistical distribution *cf* e.g. Figure 7 for neat PMMA.



381 **Figure 7.** Cell size distributions of the foams produced from neat PMMA. As discussed further below, the sample
 382 saturated at 60°C and foamed using a PDR of 30 MPa.s⁻¹ is bimodal (see Figure 5). The two modes (small vs.
 383 large size) of the cell size distribution were specified relying on a filtering procedure similar to that described in
 384 the legend of Figure 4.

385

386 Morphological characteristics of the foams from neat PMMA including average cell size, cell number
 387 density and nuclei number density were derived from the calculated cell size distributions in Figure 7.
 388 These characteristics are compiled in Table 3.

389

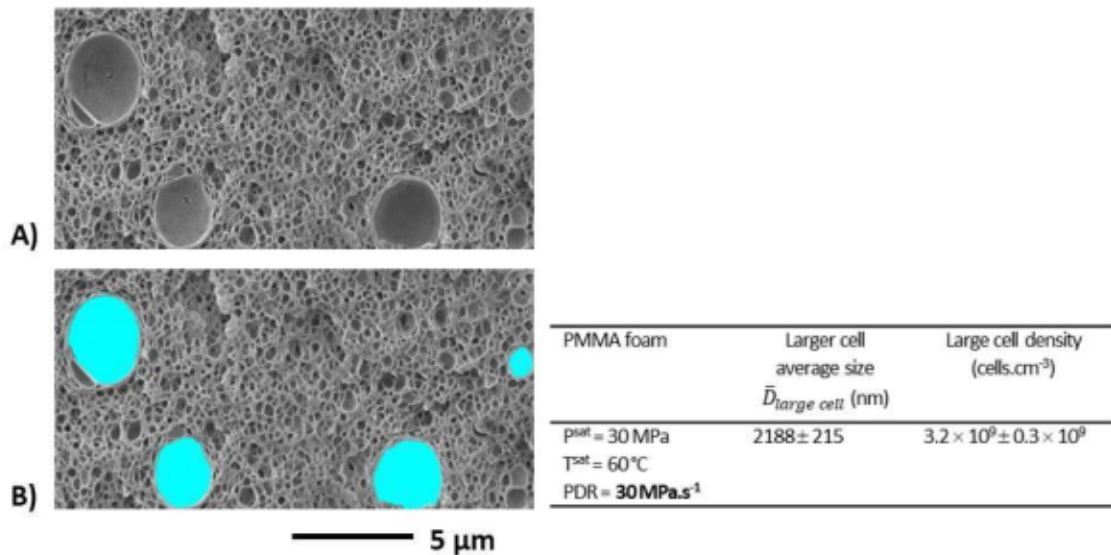
390 **Table 3.** Neat PMMA foams morphological characteristics determined by quantitative image analysis.

PMMA Foam	Foam density ρ_f (g.cm ⁻³)	Average cell size \bar{D}_{cell} (nm)	Cell density N_{cell} (cells.cm ⁻³)	Nuclei density $N_0 = N_{cell} \times \rho_s / \rho_f$ (nuclei.cm ⁻³)
$P^{sat} = 20$ MPa $T^{sat} = 40$ °C PDR = 0.3 MPa.s ⁻¹	0.78 ± 0.05	1900 ± 46	$3.2 \times 10^{10} \pm 0.6 \times 10^{10}$	$4.8 \times 10^{10} \pm 1.2 \times 10^{10}$

$P^{sat} = 20 \text{ MPa}$ $T^{sat} = 60 \text{ }^\circ\text{C}$ PDR = 0.3 MPa.s⁻¹	0.81 ± 0.03	4340 ± 119	$4.2 \times 10^9 \pm 0.3 \times 10^9$	$6.1 \times 10^9 \pm 0.7 \times 10^9$
$P^{sat} = 30 \text{ MPa}$ $T^{sat} = 40 \text{ }^\circ\text{C}$ PDR = 0.5 MPa.s⁻¹	0.76 ± 0.09	2070 ± 43	$3.3 \times 10^{10} \pm 0.1 \times 10^{10}$	$5.1 \times 10^{10} \pm 0.8 \times 10^{10}$
$P^{sat} = 30 \text{ MPa}$ $T^{sat} = 60 \text{ }^\circ\text{C}$ PDR = 0.5 MPa.s⁻¹	0.6 ± 0.02	2892 ± 60	$1.6 \times 10^{10} \pm 0.2 \times 10^{10}$	$3.1 \times 10^{10} \pm 0.5 \times 10^{10}$
$P^{sat} = 20 \text{ MPa}$ $T^{sat} = 40 \text{ }^\circ\text{C}$ PDR = 4 MPa.s⁻¹	0.64 ± 0.01	1867 ± 61	$5.9 \times 10^{10} \pm 2.0 \times 10^{10}$	$1.1 \times 10^{11} \pm 0.4 \times 10^{11}$
$P^{sat} = 20 \text{ MPa}$ $T^{sat} = 60 \text{ }^\circ\text{C}$ PDR = 4 MPa.s⁻¹	0.52 ± 0.003	4373 ± 299	$4.9 \times 10^9 \pm 2.0 \times 10^9$	$1.1 \times 10^{10} \pm 0.5 \times 10^{10}$
$P^{sat} = 30 \text{ MPa}$ $T^{sat} = 40 \text{ }^\circ\text{C}$ PDR = 30 MPa.s⁻¹	0.53 ± 0.003	231 ± 10	$2.1 \times 10^{13} \pm 0.2 \times 10^{13}$	$4.6 \times 10^{13} \pm 0.5 \times 10^{13}$
$P^{sat} = 30 \text{ MPa}$ $T^{sat} = 60 \text{ }^\circ\text{C}$ PDR = 30 MPa.s⁻¹	0.6 ± 0.01	250 ± 8	$1.8 \times 10^{13} \pm 0.1 \times 10^{13}$	$3.5 \times 10^{13} \pm 0.1 \times 10^{13}$

391

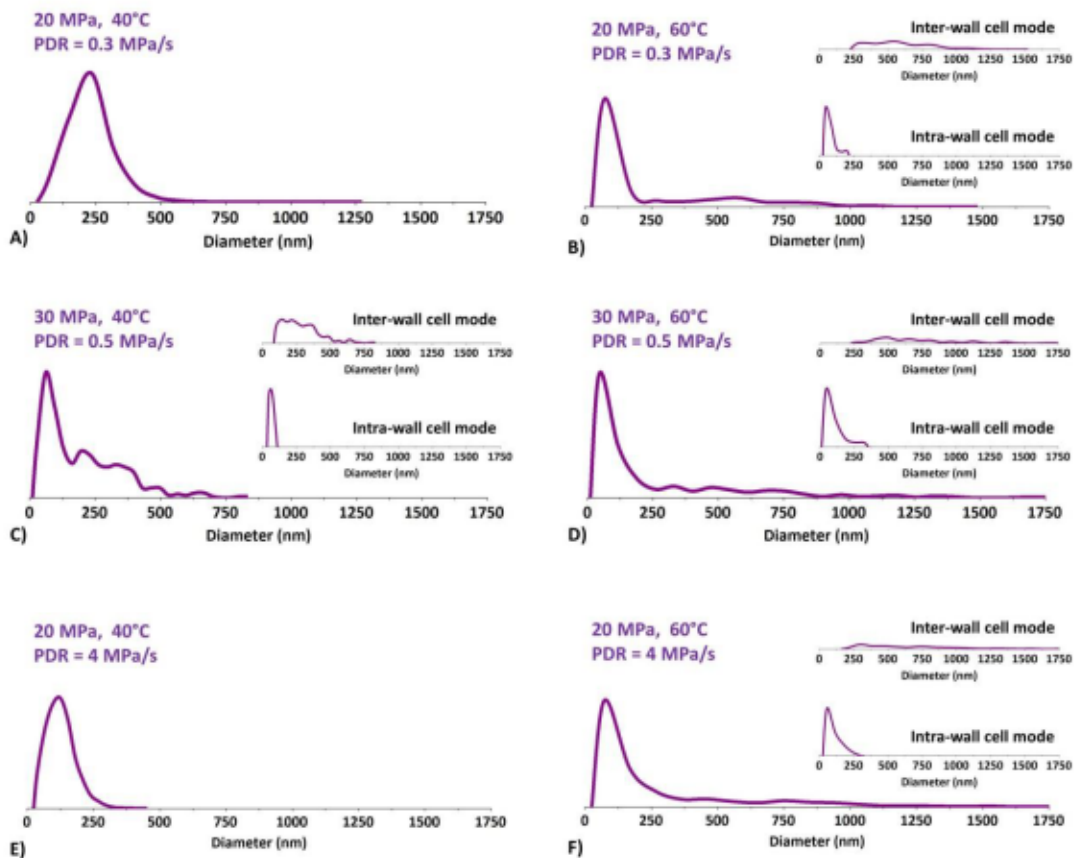
392 The PMMA foams imaged in Figure 5 are essentially « homogeneous » i.e. their cell size distributions
393 (Figure 7) are monomodal, apart from one sample saturated at 60 °C and foamed at 30 MPa.s⁻¹. This
394 sample shows two porosity populations: numerous small-sized cells and far less numerous much
395 larger cells, both dispersed in the solid lattice. For this foam, the mean cell size listed in Table 3 (last
396 row) is the weighted average of the two populations. Aided by the marked difference in size of the
397 two populations, the average size and number density of the larger cells were assessed (Figure 8) by
398 applying a connected filter (an opening by reconstruction) to the segmented/binarized image. More
399 precisely, a large-sized morphological erosion followed by a geodesic dilation of infinite size, was
400 used to discard the small cell population (Figure 8.B). This discrete (in number) large cell population
401 shall be paralleled to the systematic large cells observed at 60 °C at lower PDR (0.3 to 4 MPa.s⁻¹). In
402 other words, in the case of homogenous nucleation, a PDR as high as 30 MPa.s⁻¹ is not high enough
403 to suppress totally the impact of temperature upon the final foam structure. As mentioned earlier,
404 the situation is different in the case of heterogeneous nucleation, where the saturation temperature
405 no longer influences the final foam structure, which is only controlled by such a high PDR (30 MPa.s⁻¹).
406 ¹).

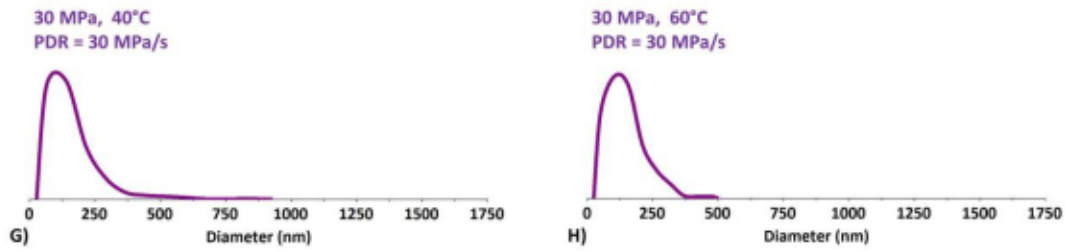


407

408 **Figure 8.** Local illustration of the segmentation (binarization) of the large cell population of the PMMA foam
 409 saturated at 60 °C and foamed at a high PDR of 30 MPa.s⁻¹.

410 Quite interestingly, PMMA/10 wt% MAM foams reveal a cell size bimodality in the majority of the
 411 samples up to a PDR of 4 MPa.s⁻¹. The cell size distributions (Figure 9) and associated morphological
 412 characteristics (Table 4) were first determined considering all cells with no distinction.





413

414 **Figure 9.** Cell size distributions of the foams produced from 90/10 PMMA/MAM blends. Refer to Figure 4 for a
 415 more complete legend.

416 Then, for bimodal samples, small porosities, referred to as intra skeletal pores, localized within locally
 417 thicker struts and inter-cell walls were distinguished from inter skeletal pores. Using the image
 418 analysis procedures described in Section 2.4 cf e.g. Figure 3.B, the two modes of the global cell size
 419 distributions were determined (Figure 9). The mean diameter of each cell mode is given in Table 5
 420 along with the inter-wall cell fraction (%).

421 **Table 4.** PMMA 10 wt% MAM foams morphological characteristics determined by quantitative image analysis.

PMMA/10 wt% MAM Foam	Foam density ρ_f (g.cm ⁻³)	Average cell size \bar{D}_{cell} (nm)	Cell density N_{cell} (cells.cm ⁻³)	Nuclei density $N_0 = N_{cell} \times \rho_s / \rho_f$ (nuclei.cm ⁻³)	Number of modes
$P^{s:st} = 20$ MPa $T^{s:st} = 40$ °C PDR = 0.3 MPa.s⁻¹	0.85 ± 0.002	228 ± 3	$1.2 \times 10^{13} \pm 0.1 \times 10^{13}$	$1.7 \times 10^{13} \pm 0.2 \times 10^{13}$	Very slightly bimodal*
$P^{s:st} = 20$ MPa $T^{s:st} = 60$ °C PDR = 0.3 MPa.s⁻¹	0.67 ± 0.01	206 ± 5	$1.0 \times 10^{13} \pm 0.2 \times 10^{13}$	$1.8 \times 10^{13} \pm 0.5 \times 10^{13}$	Bimodal
$P^{s:st} = 30$ MPa $T^{s:st} = 40$ °C PDR = 0.5 MPa.s⁻¹	0.66 ± 0.01	193 ± 4	$3.6 \times 10^{13} \pm 0.2 \times 10^{13}$	$6.5 \times 10^{13} \pm 0.8 \times 10^{13}$	Bimodal
$P^{s:st} = 30$ MPa $T^{s:st} = 60$ °C PDR = 0.5 MPa.s⁻¹	0.53 ± 0.01	239 ± 57	$1.5 \times 10^{13} \pm 0.5 \times 10^{13}$	$3.4 \times 10^{13} \pm 1.4 \times 10^{13}$	Bimodal
$P^{s:st} = 20$ MPa $T^{s:st} = 40$ °C PDR = 4 MPa.s⁻¹	0.59 ± 0.01	126 ± 4	$5.2 \times 10^{13} \pm 2.1 \times 10^{13}$	$1.0 \times 10^{14} \pm 0.5 \times 10^{14}$	Monomodal
$P^{s:st} = 20$ MPa $T^{s:st} = 60$ °C PDR = 4 MPa.s⁻¹	0.52 ± 0.02	260 ± 20	$1.4 \times 10^{13} \pm 0.4 \times 10^{13}$	$3.2 \times 10^{13} \pm 1.2 \times 10^{13}$	Bimodal
$P^{s:st} = 30$ MPa $T^{s:st} = 40$ °C PDR = 30 MPa.s⁻¹	0.52 ± 0.004	152 ± 6	$7.9 \times 10^{13} \pm 0.6 \times 10^{13}$	$1.8 \times 10^{14} \pm 0.3 \times 10^{14}$	Monomodal
$P^{s:st} = 30$ MPa $T^{s:st} = 60$ °C PDR = 30 MPa.s⁻¹	0.51 ± 0.001	143 ± 3	$9.3 \times 10^{13} \pm 1.3 \times 10^{13}$	$2.2 \times 10^{14} \pm 0.4 \times 10^{14}$	Monomodal

422 *Foam samples produced at 40 °C and at the lowest pressure drop (0.3 MPa.s⁻¹) were very locally typified by thick walls and struts
 423 showing a discrete nano-scaled porosity. Such local areas being so few, those samples were considered as (essentially) monomodal.

424

425 **Table 5.** Some of the foams produced from 90/10 PMMA/MAM solid blend showed clearly two scales of
 426 porosity i.e. nano-sized intra-wall cells versus micro-sized inter-wall cells. The inter-wall cell fraction was
 427 calculated as the inter-cell number to total cell number.

PMMA/10 wt% MAM Foam	Average intra-wall cell size $\bar{D}_{intra-wall cell}$ (nm)	Average inter-wall cell size $\bar{D}_{inter-wall cell}$ (nm)	Inter-wall cell fraction (%)
----------------------	---	---	------------------------------

$P^{sat} = 20 \text{ MPa}$ $T^{sat} = 60 \text{ }^\circ\text{C}$ PDR = 0.3 MPa.s⁻¹	76 ± 4	572 ± 6	24 ± 1
$P^{sat} = 30 \text{ MPa}$ $T^{sat} = 40 \text{ }^\circ\text{C}$ PDR = 0.5 MPa.s⁻¹	65 ± 5	277 ± 3	60 ± 1
$P^{sat} = 30 \text{ MPa}$ $T^{sat} = 60 \text{ }^\circ\text{C}$ PDR = 0.5 MPa.s⁻¹	95 ± 4	671 ± 18	25 ± 9
$P^{sat} = 20 \text{ MPa}$ $T^{sat} = 60 \text{ }^\circ\text{C}$ PDR = 4 MPa.s⁻¹	95 ± 4	658 ± 21	29 ± 2

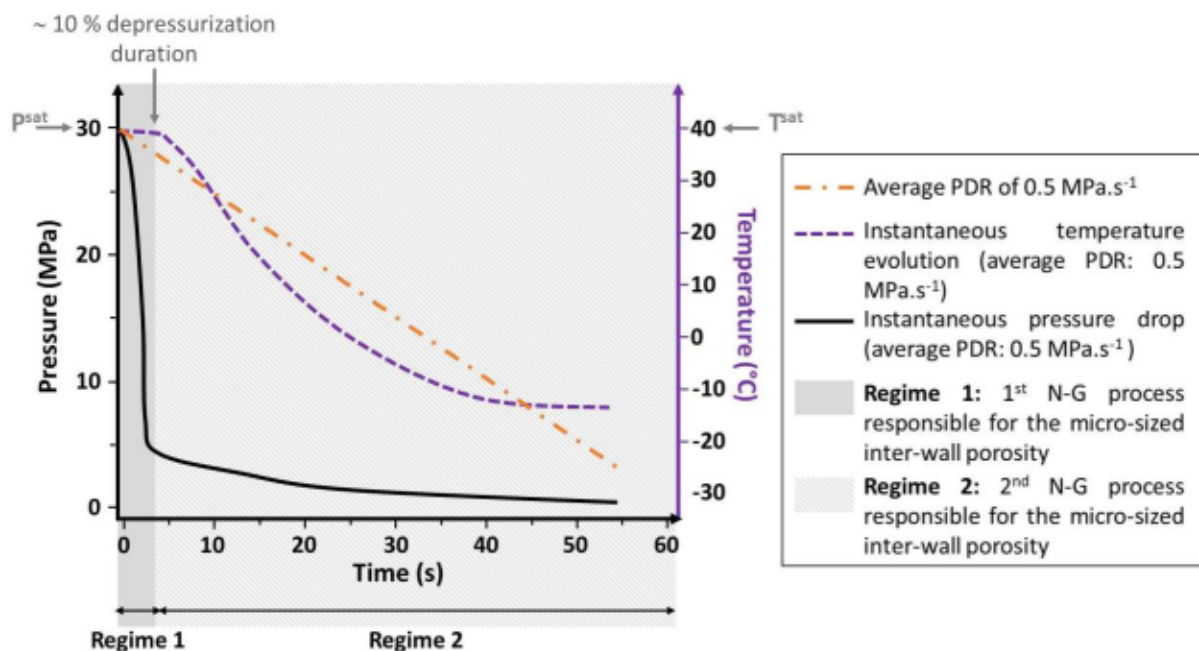
428

429 To the authors' knowledge, this is the first time such a double porosity is mentioned and quantified
430 in PMMA/MAM acrylic micro-nano foams. The intra-skeletal pores appear as a reproducible sub
431 population of nano pores with an average diameter ranging from 65 to 95 nm (Table 5). One
432 candidate explanation may be that bimodal foams are formed by a twofold separation process *i.e.* two
433 successive nucleation growth (N-G) processes. The first to occur is the expected or « classical » N-G process.
434 The second N-G process would occur during a subsequent second foaming step inside still CO₂-filled MAM
435 micellar objects within the walls. In other words, residual CO₂ in micellar objects enables a second
436 foaming and therefore, an intra skeletal true nano porosity. The reason for this may be that the PDR
437 at which the pressure is released is actually uncontrolled and shall be regarded as an average PDR. To
438 be more precise, a PDR of 0.5 MPa.s⁻¹ shall read as *an average* PDR (APDR) of 0.5 MPa.s⁻¹. Using an
439 APDR of 0.5 MPa.s⁻¹, Pinto et al. [40] have measured the evolution of the instantaneous pressure and
440 temperature during the depressurization stage (see Figure 8 of their paper). During the early stages
441 (in the first seconds) of the depressurization, the system temperature stays around T^{sat} , while
442 pressure decreases abruptly at an instantaneous rate far higher (by almost one order of magnitude)
443 than the APDR (Figure 10). These early stages, typified by a high temperature and a high
444 instantaneous PDR, originate the aforementioned first expected N-G process (whereby MAM
445 nanostructures act as effective nucleants) responsible for the inter-skeletal cell population. After
446 these early stages, the depressurization stage continues with a regular drop of the vessel
447 temperature (down to values below RT), while instantaneous pressure decreases (towards ambient
448 pressure) at a much slower instantaneous rate, say one order of magnitude lower than the APDR
449 (Figure 10). Where the first N-G process occurred, the effective glass transition temperature of the
450 PMMA matrix T_g^{ef} has rapidly raised (due to CO₂ release during the first N-G process) and the system
451 is therefore locally vitrified. The second N-G process responsible for the intra-skeletal nano-cell
452 population is going to develop independently of the first N-G process, in local areas where residual
453 CO₂ is still available. The slow instantaneous PDR, the effective temperature and the effective glass
454 temperature are less favorable. Cell growth is thus minimized. Due to the very low effective

455 (instantaneous) PDR (Figure 10), only MAM nanostructures still concentrating the blowing agent can
 456 nucleate [8]. Recall that using scCO₂ Arora et al. [41] produced bimodal foams from a polystyrene
 457 precursor by reducing the pressure in stages. The marked slope change in instantaneous pressure
 458 decrease that typifies the pressure release in our study (*i.e.* steep decrease during the early stage of
 459 the depressurization followed by an almost asymptotic behavior down to ambient pressure (Figure
 460 10)) shall be paralleled to a pressure reduction in stages.

461 *As always*, the depressurization step most likely induces local temperature and pressure gradients.
 462 The information recorded by *punctual* pressure and temperature sensors, as schematically
 463 represented in Figure 10, is by definition sensitive to such gradients. Yet, the main trends discussed
 464 in this work *i.e.* *i)* a first regime typified by a nearly constant effective temperature $T^{ef}(t)$ and an
 465 instantaneous PDR $\frac{dP(t)}{dt}$ one order of magnitude higher than the APDR and *ii)* a second regime
 466 characterized by a regular drop of $T^{ef}(t)$ and a pressure decrease $\frac{dP(t)}{dt}$ one order of magnitude
 467 smaller than the APDR, remain true at the sample-scale, irrespective of local gradients.

468 As the APDR is increased, the first N-G process implies more and more MAM nanostructures so that
 469 ultimately (at 30 MPa.s⁻¹ in our work) there is no MAM nucleants left for a second N-G process.



470
 471 **Figure 10.** Schematic representation of the instantaneous (true) pressure and temperature evolution during a
 472 depressurization process of average PDR (APDR) equal to 0.5 MP.s⁻¹. Modified from original experimental work
 473 by Pinto et al. [40] using the same high-pressure vessel and the same operating conditions than in this study.

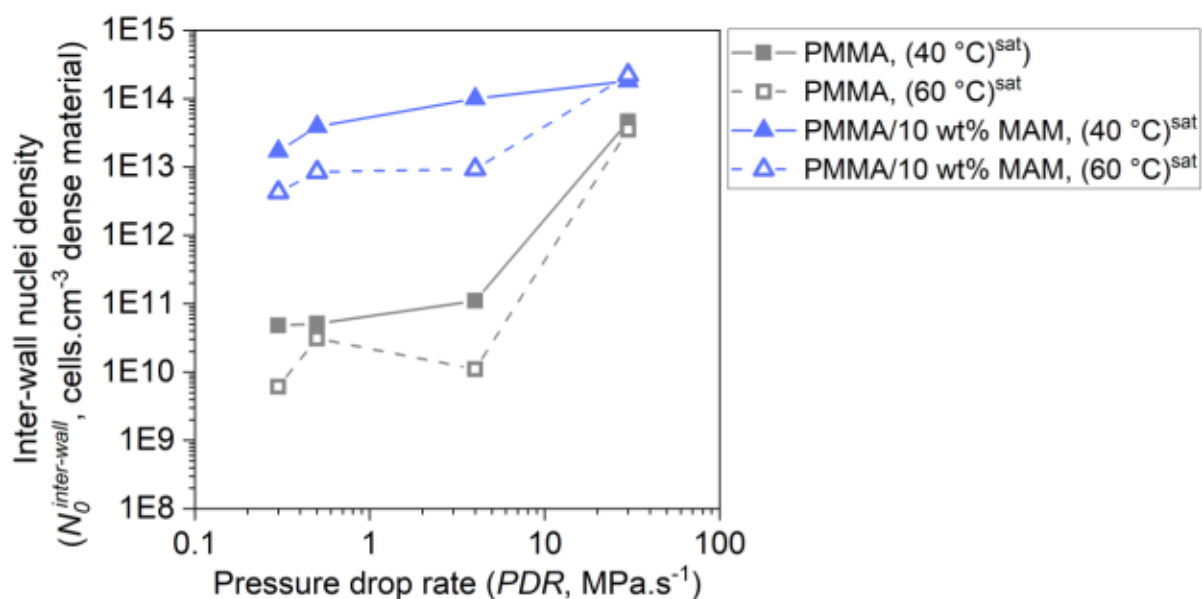
474

475 In our view, the bimodal blend foams observed in this study essentially when using an average PDR in
 476 the range 0.3 – 4 MPa.s⁻¹ shall not be designated as « heterogeneous ». They should rather be
 477 described as « doubly homogeneous ». Indeed, the dynamics of the vessel pressure and temperature
 478 evolution during the depressurization step produces two N-G processes that develop in two
 479 successive stages, independently of one another. In each N-G process, the block copolymer (BCP)
 480 does homogenize the foam structure.

481

482 In Figure 11, the inter-wall nuclei density, noted $N_0^{inter-wall}$ (see the legend of Figure 11), is plotted
 483 as a function of the average PDR (APDR) using a bi logarithmic scale. $N_0^{inter-wall}$ increases as the
 484 APDR is incremented with a threshold effect at 4 MPa.s⁻¹. The threshold effect is less marked in the
 485 foams from 90/10 PMMA/MAM blend saturated at 40°C. The rise of $N_0^{inter-wall}$ as the APDR is
 486 increased is much smoother in the foams from PMMA/MAM than in the foams from neat PMMA.
 487 This demonstrates again the homogenizing role of an organic BCP such as MAM, which triggers high
 488 inter-wall nuclei densities even at low APDR. Using PS or PS/talc systems, Tammaro et al. [24] made
 489 similar log-log plots in which the nuclei density linearly increases with APDR. The smoothing effect
 490 observed with MAM organic additive is less pronounced with talc inorganic additive. This may be
 491 related to the fact that in Tammaro et al. [24], the PS or PS/talc systems are in molten (flowing) state,
 492 while our PMMA and PMMA/MAM systems are in a true (non-flowing) solid state.

493



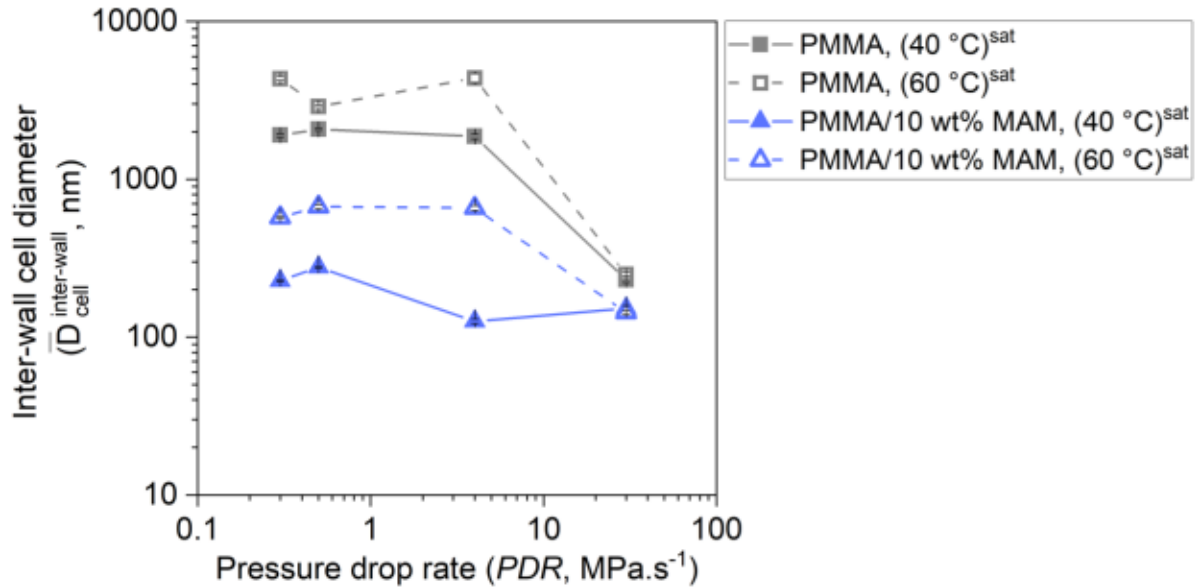
494

495 **Figure 11.** Inter-wall nuclei density (noted $N_0^{inter-wall}$) as a function of average PDR (APDR) over 2 decades
 496 ranging from 0.3 MPa.s⁻¹ to 30 MPa.s⁻¹ in a bi logarithmic scale. In monomodal samples, the inter-wall nuclei
 497 density is the usual nuclei density referred to as N_0 in Table 3 and Table 4. In bimodal foam samples (produced
 498 from 90/10 PMMA/MAM blend), $N_0^{inter-wall}$ is equal to N_0 multiplied by the Inter-wall cell fraction (Table 5).
 499 Saturation temperature is 40 °C or 60°C.

500

501 As for the inter-wall nuclei density, the inter-wall cell mean diameter ($\bar{D}_{inter-wall\ cell}$) (Figure 12) is
502 discriminated by APDR, saturation temperature and MAM presence.

503



504

505 **Figure 12.** Mean inter-wall cell size as a function of average PDR (APDR); saturation temperature 40 °C or 60 °C,
506 PMMA and PMMA/10 wt% MAM. In monomodal foam samples, the inter-wall cell mean diameter
507 $\bar{D}_{inter-wall\ cell}$ is the average cell diameter \bar{D}_{cell} listed in Table 3 and Table 4.

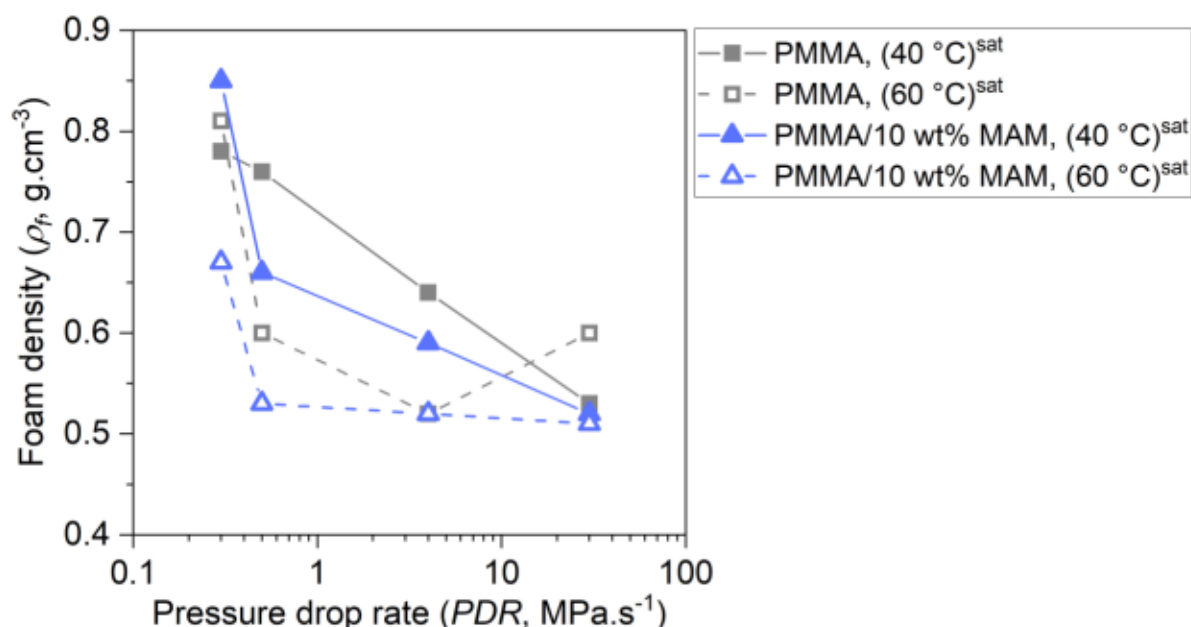
508

509 Over low to intermediate APDR (0.3 to 4 MPa.s⁻¹), MAM enables a gain of 3 decades in $N_0^{Inter-wall}$
510 and a gain of one decade in $\bar{D}_{inter-wall\ cell}$ at fixed saturation temperature (read from the bottom
511 up Figures 11 and 12). Without MAM addition, the APDR is the main factor (the driving force)
512 explaining the reduction by two orders of magnitude of the inter-wall cell diameter (read from left to
513 right Figure 12). With MAM, the APDR appears of secondary importance in the reduction of the
514 porosity dimensions (at a fixed temperature, the inter-wall cell diameter being reduced no more than
515 by a factor two or three; read from left to right Figure 12).

516 At very high APDR (30 MPa.s⁻¹), the inter-wall nuclei density (Figure 11) and the inter-wall cell
517 diameter (Figure 12) both tend towards similar values without and with MAM addition. This
518 convergence actually expresses different physical phenomena in the case of neat PMMA and in the
519 case of the PMMA/MAM blend. In the former instance, the nuclei density is augmented by a physical
520 phenomenon *i.e.* a steep pressure drop. In the latter case, nucleation is essentially promoted by the
521 concentrating effect of MAM on scCO₂.

522 To our knowledge, the above influence of the APDR upon the final foam structure has been only
 523 reported in foaming experiments from the molten state, and not from the solid state as is the case
 524 here.

525 As the APDR is increased, the density (ρ_f) of our acrylic foams also decreases moderately in a
 526 comparable manner regardless of the system and the saturation temperature (Figure 13). Although
 527 the density remains rather high for foams ($> 0.5 \text{ g.cm}^{-3}$), the concomitant decrease of cell diameter
 528 (Figure 12) and ρ_f (Figure 13) in a one-step solid-state foaming of *amorphous* acrylics may be viewed
 529 as a novelty to the best of our knowledge.



530
 531 **Figure 13.** Evolution of the foam density with the average pressure drop rate (APDR) for neat PMMA and
 532 PMMA/10 wt% MAM at two saturation temperatures (40°C and 60 °C).

533
 534 Altogether, the trends contained in Figure 11, Figure 12 and Figure 13 can be attributed to the
 535 interplay of several kinetics or kinetic factors whose respective effects cannot be unraveled:
 536 evolution with time of T^{ef} and that of T_g^{ef} . More precisely, in a one-step procedure, foaming occurs
 537 inside the autoclave and the sample effective temperature (T^{ef}) is not controlled right after foaming
 538 is triggered. Indeed, depressurization induces a rapid decrease of the sample temperature (T^{ef}), the
 539 kinetics of which is not controlled [6],[42],[43] (Figure 10). However, at a certain time of cells
 540 development, the actual temperature (T^{ef}) crosses inevitably the effective glass transition
 541 temperature of the system (T_g^{ef}), either up or down. At foaming, T_g^{ef} can be much lower than that of
 542 neat PMMA before saturation [44]. When $T^{ef} < T_g^{ef}$, the cells are stabilized, this is the vitrification
 543 kinetics. Other kinetics may be interfering: phase separation and growth kinetics, kinetics of gas

544 diffusion (either through the bulk matrix phase, but also through interfaces, once MAM nodules are
545 created).

546 Among the above described numerous triggers for one-step foaming, a « low » CO₂ saturation
547 temperature complying with the supercritical state ($T^{sat} = 40\text{ °C}$ or 60 °C), a PMMA/MAM
548 combination material formulation and a high APDR should be obviously preferred.

549

550 3.3 Implications for high thermal insulation

551 Microsized and nanosized porous polymer foams, in particular those produced using scCO₂ as physical
552 foaming agent, are promising thermal insulation *green* materials [1],[2],[45],[46],[44],[47],[48] and for a
553 large variety of applications, including clothing and footwear industries.

554 The conventional route towards improving thermal insulation of polymer foams (porous materials made of
555 cells/walls/struts) generally consists in *i*) reducing cell size to the nanometer range in order to benefit from
556 the Knudsen effect and *ii*) increasing the expansion ratio (or porosity) since air conductivity is far lower than
557 that of the polymeric lattice [46], [47],[2],[49],[50],[51],[48],[52],[53]. This strategy aims at minimizing the
558 conductive component of the foam effective conductivity k_{ef} . Yet, decreasing cell size and increasing the
559 expansion ratio requires a high number density of cells leading to very thin struts and cell walls which,
560 unfortunately, increase ultimately the radiative transmittivity [54],[55],[48],[52]. Such an increase in the
561 radiative component of the foam effective conductivity k_{ef} often *erases* the performance gain (reduction of
562 the conductive component of k_{ef}) permitted by the Knudsen effect and a high gas fraction [48],[52].

563 Therefore, the lowered gas conductivity achieved thanks to the Knudsen effect successfully reduces the
564 effective conductivity k_{ef} only in foams showing a relatively high density (e.g $\sim 0.3\text{-}0.5\text{ g/cm}^3$) *i.e.* a rather
565 low expansion ratio [52]. The monomodal foams produced in this work from PMMA/10 wt% MAM
566 precursor at high APDR ($30\text{ MPa}\cdot\text{s}^{-1}$) after scCO₂ saturation at 40 °C or 60 °C and at moderate APDR ($4\text{ MPa}\cdot\text{s}^{-1}$)
567 after saturation at 40 °C (Figure 6) exhibit nanosized alveolar cells ($\bar{D}_{cell} < 150\text{ nm}$) and a somewhat high
568 density ($\sim 0.5\text{ g}\cdot\text{cm}^{-3}$) (table 4). According to the literature cited above and particularly in the line with
569 Buahom et al. [48] and Pang et al. [52], these foams shall show a low effective thermal conductivity.

570 Using a comprehensive predictive model validated by published experimental data in the literature, Buahom
571 et al. conclude that in low density monomodal foams, the optimal cell-size minimizing the radiative
572 transmittivity (so that the lowered gas conductivity remains meaningful) lies in the micrometer range.

573 In our view, the bimodal foams produced in our work at low to moderate APDR ($0.3\text{ MPa}\cdot\text{s}^{-1}$ to $4\text{ MPa}\cdot\text{s}^{-1}$)
574 after scCO₂ saturation at 40 °C and/or 60 °C (Figure 6 and table 5) shall represent a potential innovative
575 solution towards reducing drastically heat transfer. These bimodal samples show locally a porous solid

576 skeleton made up of thick walls and struts and including numerous well apart intra-skeleton nanopores (of a
577 size comparable to that of the micellar nanostructures in the precursor). This locally thick skeleton
578 encapsulates local domains of relatively high-expansion ratio. These local domains are formed either by
579 several adjacent submicrometer-sized cells or reduce to a single submicrometer-sized cell (referred above as
580 inter-wall pores). Within these local domains typified by a high porosity, a submicrometer cell size at which
581 the Knudsen effect starts to take place, the (local) conductive thermal conduction shall be low. At the
582 immediate periphery of these local domains, the larger amount of matter and the well apart nanopores
583 within the thick skeleton shall lower transmittivity (radiative conduction) and the conductive solid
584 conduction¹, respectively. Heat transfer shall be further minimized by the higher tortuosity of the thick
585 skeleton bordering local domains of higher expansion ratio [56],[57],[48]. In addition, the nanosized cells
586 within the thick nanoporous skeleton shall enhance phonon scattering, which increases the solid thermal
587 resistance thereby reducing the solid conductivity [58],[59],[60],[61].

588 Thus, in this series of bimodal acrylic foams, the benefit from the Knudsen effect within well expanded local
589 domains showing porosity dimensions in the submicrometer range remains meaningful thanks to a locally
590 poorly expanded nanoporous thick solid skeleton *encapsulating* these local domains and preventing
591 radiative thermal conduction from overriding the conductive component at the sample scale.

592 This suggests that micro-nano bimodal foams may represent better candidates for improved thermal
593 insulation than « all nanosized » foams.

594 The next step will be to measure the effective conductivity of these thermal insulator polymeric foams. Yet,
595 as recently stressed by Sánchez-Calderón et al. [62], the accurate measurement of the thermal conductivity
596 of micro-nanocellular polymers is quite a challenge which is beyond the scope of the current contribution.

597

598 **4. Conclusion**

599 With the target of achieving micro-nano foams, this study principally addresses the combined
600 beneficial effects of block copolymer (BCP) addition and high average pressure drop rate (APDR) in
601 one-step solid-state batch scCO₂ foaming. Producing micro-nano foams is a multi-factorial issue,
602 where numerous subtle parameters interplay and compete; one can quote the saturation conditions
603 *i.e.* P^{sat} and T^{sat} , the material effective temperature during foaming $T^{ef}(t)$, the effective glass
604 transition temperature of the plasticized system $T_g^{ef}(t)$, the APDR value, and the presence of block
605 copolymer.

606 APDR and BCP are two key triggering factors. Either parameter may become prevalent for ruling the
607 cell size and the overall density. Over the scrutinized range of saturation temperature (40 °C and 60

¹ Heat conduction in the solid is reduced by the significant Knudsen effect in well apart nanopores.

608 °C), the APDR is the main factor for significantly reducing cell size and increasing nuclei density in
609 foams from neat PMMA. In the block copolymer approach, increasing the APDR appears of secondary
610 importance as the targeted reduction of the porosity dimensions and augmentation of the nuclei
611 density are essentially the consequence of the MAM presence. Yet, in this latter case, increasing the
612 APDR still promotes the « efficiency » of BCP nucleants. In particular, a real efficient nucleation
613 activity of MAM additive is observed at very high average APDR (30 MPa.s⁻¹), leading to unimodal
614 homogeneous distribution of tiny pores, typically 150 nm in diameter, in nearly nanosized foams.
615 Next, in our saturation conditions ('low' temperature complying with the supercritical state for CO₂), a
616 high APDR tends to reduce also foam density (although in a moderate way, 0.8 down to 0.5 g.cm⁻³).
617 Let us insist again on the fact that in the block copolymer approach, the average PDR (APDR) plays
618 only 'a supporting role' in the final structure of the foam. More precisely, a APDR increment
619 promotes the efficiency of the BCP nucleants. This interplay between BCP and APDR, combined with
620 the underlying instantaneous dynamics dP/dt of the apparent average APDR $\Delta P/\Delta t$, which can be
621 paralleled to a two-stage pressure reduction, can be used to produce bimodal foams where a truly
622 intra-wall/intra-strut nanosized porosity is distinguished from the inter-wall micro-sized pores.
623 Indeed, the evolution with time of the uncontrolled instantaneous depressurization rate dP/dt
624 (Figure 10) leads to two serial nucleation-growth (N-G) processes. Such two N-G processes develop
625 independently of one another. As the (apparent) average PDR ($\Delta P/\Delta t$) is higher (as nucleation occurs
626 over a shorter time interval), the earliest N-G process is all the more important to the detriment of
627 the second N-G process, which ends by running out at very high APDR 30 (MPa.s⁻¹). Last we provide
628 some arguments in favor of the superiority of these twofold porosity foams (rather than 'all nano
629 foams') in applications requiring thermal insulation. Indeed, in these double porosity foams, benefit
630 from the Knudsen effect, achieved within well expanded local domains showing submicrometer
631 pores, would remain meaningful thanks to a locally poorly expanded nanoporous thick solid skeleton
632 encapsulating these local domains. Such local encapsulation prevents radiative thermal conduction
633 from overriding the conductive component at the sample scale.

634

635 **ACKNOWLEDGMENTS** This work was supported by the Agence Nationale de la Recherche (ANR,
636 France); grant number AAPG PRCE 2018CE06 0030, 2019; ANR is gratefully acknowledged.

637

638 5. References

- 639 1. Li, T.; Zhao, G.; Wang, G.; Zhang, L.; Hou, J. Thermal-insulation, Electrical, and Mechanical Properties of Highly-
640 expanded PMMA/MWCNT Nanocomposite Foams Fabricated by Supercritical CO₂ Foaming. *Macromol. Mater. Eng.*
641 **2019**, *304*, 1800789, doi:10.1002/mame.201800789.
- 642 2. Notario, B.; Pinto, J.; Solorzano, E.; de Saja, J.A.; Dumon, M.; Rodríguez-Pérez, M.A. Experimental Validation of the
643 Knudsen Effect in Nanocellular Polymeric Foams. *Polymer* **2015**, *56*, 57–67, doi:10.1016/j.polymer.2014.10.006.
- 644 3. Coste, G.; Negrell, C.; Caillol, S. From Gas Release to Foam Synthesis, the Second Breath of Blowing Agents. *European*
645 *Polymer Journal* **2020**, *140*, 110029, doi:10.1016/j.eurpolymj.2020.110029.

- 646 4. Park, C.B.; Behraves, A.H.; Venter, R.D. Low Density Microcellular Foam Processing in Extrusion Using CO₂. *Polymer*
647 *Engineering & Science* **1998**, *38*, 1812–1823, doi:10.1002/pen.10351.
- 648 5. Magjarevic, R.; Wu, H.; Krampe, E.; Schlicht, H.; Wintermantel, E. Application of a Microcellular Injection Molding
649 Process (MuCell®) to Produce an Implant with Porous Structure.; Dössel, O., Schlegel, W.C., Eds.; IFMBE Proceedings:
650 Munich, Germany, **2009**; Vol. 25, pp. 61–64.
- 651 6. Dumon, M.; Ruiz, J.A.R.; Sanz, J.P.; Perez, M.A.R.; Tallon, J.-M.; Pedros, M.; Cloutet, E.; Viot, P. Block Copolymer-
652 Assisted Microcellular Supercritical CO₂ Foaming of Polymers and Blends. *Cellular Polymers* **2012**, *31*, 207–222,
653 doi:10.1177/026248931203100402.
- 654 7. Nalawade, S.P.; Picchioni, F.; Janssen, L.P.B.M. Supercritical Carbon Dioxide as a Green Solvent for Processing
655 Polymer Melts: Processing Aspects and Applications. *Progress in Polymer Science* **2006**, *31*, 19–43,
656 doi:10.1016/j.progpolymsci.2005.08.002.
- 657 8. Haurat, M.; Dumon, M. Amorphous Polymers' Foaming and Blends with Organic Foaming-Aid Structured Additives in
658 Supercritical CO₂, a Way to Fabricate Porous Polymers from Macro to Nano Porosities in Batch or Continuous
659 Processes. *Molecules* **2020**, *25*, 5320, doi:10.3390/molecules25225320.
- 660 9. Haurat, M.; Tassaing, T.; Dumon, M. FTIR in Situ Measurement of Swelling and CO₂ Sorption in Acrylic Polymers at
661 High CO₂ Pressures. *The Journal of Supercritical Fluids* **2022**, *182*, 105534, doi:10.1016/j.supflu.2022.105534.
- 662 10. Spitael, P.; Macosko, C.W.; McClurg, R.B. Block Copolymer Micelles for Nucleation of Microcellular Thermoplastic
663 Foams. *Macromolecules* **2004**, *37*, 6874–6882, doi:10.1021/ma049712q.
- 664 11. Pinto, J.; Dumon, M.; Pedros, M.; Reglero, J.; Rodriguez-Perez, M.A. Nanocellular CO₂ Foaming of PMMA Assisted by
665 Block Copolymer Nanostructure. *Chemical Engineering Journal* **2014**, *243*, 428–435,
666 doi:10.1016/j.cej.2014.01.021.
- 667 12. Bernardo, V.; Martin-de Leon, J.; Pinto, J.; Catelani, T.; Athanassiou, A.; Rodriguez-Perez, M.A. Low-Density
668 PMMA/MAM Nanocellular Polymers Using Low MAM Contents: Production and Characterization. *Polymer* **2019**, *163*,
669 115–124, doi:10.1016/j.polymer.2018.12.057.
- 670 13. Bernardo, V.; Martin-de Leon, J.; Rodriguez-Perez, M.A. Highly Anisotropic Nanocellular Polymers Based on Tri-Phase
671 Blends of PMMA with Two Nucleating Agents. *Materials Letters* **2019**, *255*, 126587,
672 doi:10.1016/j.matlet.2019.126587.
- 673 14. Costeux, S.; Foether, D. Continuous Extrusion of Nanocellular Foams. In Proceedings of the Conference proceedings
674 Annual Technical Conference-ANTEC; Orlando, **2015**; pp. 2740–2745.
- 675 15. Gómez-Monterde, J.; Hain, J.; Sánchez-Soto, M.; Maspoch, M.L. Microcellular Injection Moulding: A Comparison
676 between MuCell Process and the Novel Micro-Foaming Technology IQ Foam. *Journal of Materials Processing*
677 *Technology* **2019**, *268*, 162–170, doi:10.1016/j.jmatprotec.2019.01.015.
- 678 16. León, J.M.; Bernardo, V.; Rodríguez-Pérez, M.Á. Key Production Parameters to Obtain Transparent Nanocellular
679 PMMA. *Macromolecular Materials and Engineering* **2017**, *5*, doi:10.1002/mame.201700343.
- 680 17. Goel, S.K.; Beckman, E.J. Generation of Microcellular Polymeric Foams Using Supercritical Carbon Dioxide. I: Effect of
681 Pressure and Temperature on Nucleation. *Polymer Engineering and Science* **1994**, *34*, 1137–1147,
682 doi:10.1002/pen.760341407.
- 683 18. Ruiz, J.A.R.; Pedros, M.; Tallon, J.-M.; Dumon, M. Micro and Nano Cellular Amorphous Polymers (PMMA, PS) in
684 Supercritical CO₂ Assisted by Nanostructured CO₂-Phylic Block Copolymers – One Step Foaming Process. *The Journal*
685 *of Supercritical Fluids* **2011**, *58*, 168–176, doi:10.1016/j.supflu.2011.04.022.
- 686 19. Tammaro, D.; Contaldi, V.; Carbone, M.P.; Di Maio, E.; Iannace, S. A Novel Lab-Scale Batch Foaming Equipment: The
687 Mini-Batch. *Journal of Cellular Plastics* **2016**, *52*, 533–543, doi:10.1177/0021955X15584654.
- 688 20. Taki, K. Experimental and Numerical Studies on the Effects of Pressure Release Rate on Number Density of Bubbles
689 and Bubble Growth in a Polymeric Foaming Process. *Chemical Engineering Science* **2008**, *63*, 3643–3653,
690 doi:10.1016/j.ces.2008.04.037.
- 691 21. Khan, I.; Costeux, S.; Adrian, D.; Bunker, S. Numerical Studies of Nucleation and Bubble Growth in Thermoplastic
692 Foams at High Nucleation Rates.; Dow Chemical Co., Midland, MI (United States); Seattle, WA (United States), **2013**.
- 693 22. Guo, Q.; Mei, Y.; Chang, S.S.Y.; Wang, J.; Park, C.B. Cell Nucleation and Growth Study of PP Foaming with CO₂ in a
694 Batch-Simulation System. *SAE Technical Paper Series* **2006**, doi:10.4271/2006-01-0507.
- 695 23. Tammaro, D.; Iannace, S.; Di Maio, E. Insight into Bubble Nucleation at High-Pressure Drop Rate. *Journal of Cellular*
696 *Plastics* **2017**, *53*, 551–560, doi:10.1177/0021955X17695094.
- 697 24. Tammaro, D.; Astarita, A.; Di Maio, E.; Iannace, S. Polystyrene Foaming at High Pressure Drop Rates. *Industrial &*
698 *Engineering Chemistry Research* **2016**, *55*, 5696–5701, doi:10.1021/acs.iecr.5b04911.
- 699 25. Chen, L.; Sheth, H.; Wang, X. Effects of Shear Stress and Pressure Drop Rate on Microcellular Foaming Process. **2001**,
700 *37*, 12, doi:10.1106/VHC8-33K7-M1C7-0M2H.
- 701 26. Guo, Q.; Wang, J.; Park, C.B.; Ohshima, M. A Microcellular Foaming Simulation System with a High Pressure-Drop
702 Rate. *Industrial and Engineering Chemistry Research* **2006**, *45*, 6153–6161, doi:10.1021/ie060105w.
- 703 27. Shi, B.S.; Li, B.; Nan, Q.Z.; Qin, X.M. Effect of Processing Parameters on Cell Morphology of Polycarbonate Foam.
704 *Plastics, Rubber and Composites* **2011**, *40*, 457–464, doi:10.1179/1743289811Y.0000000004.
- 705 28. Muratani, K.; Shimbo, M.; Miyano, Y. Correlation of Decompression Time and Foaming Temperature on the Cell
706 Density of Foamed Polystyrene. *Cellular Polymers* **2005**, *24*, 15–27, doi:10.1177/026248930502400102.

- 707 29. Bernardo, V.; Martin-de Leon, J.; Laguna-Gutierrez, E.; Catelani, T.; Pinto, J.; Athanassiou, A.; Rodriguez-Perez, M.A.
708 Understanding the Role of MAM Molecular Weight in the Production of PMMA/MAM Nanocellular Polymers.
709 *Polymer* **2018**, *153*, 262–270, doi:10.1016/j.polymer.2018.08.022.
- 710 30. Witkin, A.P. Scale-Space Filtering.; Karlsruhe, Germany, 1983; pp. 1019–1022.
- 711 31. Babaud, J.; Witkin, A.P.; Baudin, M.; Duda, R.O. Uniqueness of the Gaussian Kernel for Scale-Space Filtering. In
712 Proceedings of the IEEE Transactions on Pattern Analysis and Machine Intelligence; **1986**; Vol. PAMI-8, pp. 26–33.
- 713 32. Koenderink, J.J. The Structure of Images. *Biological Cybernetics* **1984**, *50*, 363–370, doi:10.1007/BF00336961.
- 714 33. Laporterie, F.; Flouzat, G.; Amram, O. The Morphological Pyramid and Its Applications to Remote Sensing:
715 Multiresolution Data Analysis and Features Extraction. *Image Analysis and Stereology* **2002**, *21*, 49–53,
716 doi:10.5566/ias.v21.p49-53.
- 717 34. Perona, P.; Malik, J. Scale-Space and Edge Detection Using Anisotropic Diffusion. *IEEE Transactions on Pattern*
718 *Analysis and Machine Intelligence* **1990**, *12*, 629–639, doi:10.1109/34.56205.
- 719 35. Canseco, V.; Anguy, Y.; Roa, J.J.; Palomo, E. Structural and Mechanical Characterization of Graphite Foam/Phase
720 Change Material Composites. *Carbon* **2014**, *74*, 266–281, doi:10.1016/j.carbon.2014.03.031.
- 721 36. Martinez, E.; Jové Xde la Torre, F.; Santamaria, E. Unsupervised Morphological Segmentation of Objects in Contact.;
722 Grenoble, France, **1997**.
- 723 37. Legland, D.; Kiêu, K.; Devaux, M.-F. Computation of Minkowski Measures on 2D and 3D Binary Images. *Image*
724 *Analysis and Stereology* **2007**, *26*, 83–92, doi:10.5566/ias.v26.p83-92.
- 725 38. Costeux, S. CO₂-Blown Nanocellular Foams. *Journal of Applied Polymer Science* **2014**, *131*, 1–16,
726 doi:10.1002/app.41293.
- 727 39. Kaneko, K. Determination of Pore Size and Pore Size Distribution 1. Adsorbents and Catalysts. *Journal of Membrane*
728 *Science* **1994**, *96*, 59–89, doi:/10.1016/0376-7388(94)00126-X.
- 729 40. Pinto, J.; Reglero-Ruiz, J.A.; Dumon, M.; Rodriguez-Perez, M.A. Temperature Influence and CO₂ Transport in Foaming
730 Processes of Poly(Methyl Methacrylate)-Block Copolymer Nanocellular and Microcellular Foams. *The Journal of*
731 *Supercritical Fluids* **2014**, *94*, 198–205, doi:10.1016/j.supflu.2014.07.021.
- 732 41. Arora, K.A.; Lesser, A.J.; McCarthy, T.J. Preparation and Characterization of Microcellular Polystyrene Foams
733 Processed in Supercritical Carbon Dioxide. *Macromolecules* **1998**, *31*, 4614–4620, doi:10.1021/ma971811z.
- 734 42. Reglero Ruiz, J.A.; Dumon, M.; Pinto, J.; Rodriguez-Pérez, M.A. Low-Density Nanocellular Foams Produced by High-
735 Pressure Carbon Dioxide. *Macromolecular Materials and Engineering* **2011**, *296*, 752–759,
736 doi:10.1002/mame.201000346.
- 737 43. Reglero Ruiz, J.A.; Saiz-Arroyo, C.; Dumon, M.; Rodríguez-Perez, M.A.; Gonzalez, L. Production, Cellular Structure and
738 Thermal Conductivity of Microcellular (Methyl Methacrylate)-(Butyl Acrylate)-(Methyl Methacrylate) Triblock
739 Copolymers: Microcellular MAM Triblock Copolymers. *Polymer International* **2011**, *60*, 146–152,
740 doi:10.1002/pi.2931.
- 741 44. Ruiz, J.A.R.; Viot, P.; Dumon, M. Foaming Behaviour and Compressive Properties of Microcellular Nanostructured
742 Polystyrene. *Cellular Polymers* **2009**, *28*, 363–385, doi:10.1177/026248930902800601.
- 743 45. Forest C., Chaumont P., Cassagnau P., Swoboda B., Sonntag P., CO₂ nano-foaming of nanostructured PMMA. *Polymer* **2015**, *58*,
744 76–87, doi.org/10.1016/j.polymer.2014.12.048.
- 745 46. Forest, C., Chaumont, P., Cassagnau, P., Swoboda, B., Sonntag P., Polymer nano-foams for insulating applications prepared from
746 CO₂ foaming, *Prog. Polym. Sci.* **2015**, *41*, 122–145, doi.org/10.1016/j.progpolymsci.2014.07.001.
- 747 47. Notario, B., Pinto, J., Rodríguez-Perez, M. A., Nanoporous polymeric materials: A new class of materials with enhanced
748 properties. *Prog. Mater. Sci.* **2016**, *78–79*, 93–139, doi.org/10.1016/j.pmatsci.2016.02.002.
- 749 48. Buahom, P., Wang, C., Alshrah, M., Wang, G., Gong, P., Tran M.-P., Park, C. B., Wrong expectation of superinsulation behavior
750 from largely-expanded nanocellular foams. *Nanoscale*, **2020**, *12*, 13064–13085, doi.org/10.1039/d0nr01927e.
- 751 49. Rizvi, A., Chu, R. K. M., Park, C.B., Scalable fabrication of thermally insulating mechanically resilient hierarchically porous polymer
752 foams. *ACS Appl. Mater. Interfaces* **2018**, *10*(44), 38410–38417, doi.org/10.1021/acsami.8b11375.
- 753 50. Wang, G., Zhao, J., Wang, G., Mark, L. H., Park, C. B., Zhao, G., Low-density and structure-tunable microcellular PMMA foams with
754 improved thermal-insulation and compressive mechanical properties. *Eur. Polym. J.* **2017**, *95*, 382–393,
755 https://doi.org/10.1016/j.eurpolymj.2017.08.025.
- 756 51. Wang, L., He, Y., Jiang T., Zhang, X., Zhang, C., Peng, X., Morphologies and properties of epoxy/multi-walled carbon nanotube
757 nanocomposite foams prepared through the free-foaming and limited-foaming process. *Compos. Sci. Technol.* **2019**, *182*,
758 107776, https://doi.org/10.1016/j.compscitech.2019.107776
- 759 52. Pang, Y., Cao, Y., Zheng, W., Park C. B., A comprehensive review of cell structure variation and general rules for polymer
760 microcellular foam. *Chemical Engineering Journal* **2022**, *430*, 132662, https://doi.org/10.1016/j.cej.2021.132662.
- 761 53. Shi, Z., Zhao, G., Lei Zhang, L. Wang, G., Chai J., Ultralight and hydrophobic PVDF/PMMA open-cell foams with outstanding heat-
762 insulation and oil-adsorption performances fabricated by CO₂ molten foaming. *Journal of CO₂ Utilization* **2022**, *63*, 102108,
763 https://doi.org/10.1016/j.jcou.2022.102108.
- 764 54. Wang, G., Wang, C., Zhao, J., Wang, G., Park, C. B., Zhao G., Modelling of thermal transport through a nanocellular polymer foam:
765 toward the generation of a new superinsulating material. *Nanoscale* **2017**, *9*, 5996–6009,
766 doihttps://doi.org/10.1039/C7NR00327G
- 767 55. Wang, G., Wang, C., Zhao, J., Wang, G., Park C. B., Zhao G., Van De Walle W., Janssen H, Correction: Modelling of thermal
768 transport through a nanocellular polymer foam: Toward the generation of a new superinsulating material. *Nanoscale* **2018**, *10*,
769 20469–20473, doi.org/10.1039/C8NR90192A

- 770 56. Glicksman, L. R., Torpey, M. Factors governing heat transfer through closed cell foam insulation. *J. Therm. Insul.* **1989**, *12*, 257–
771 269, doi.org/10.1177/109719638901200
- 772 57. Glicksman, L. R., Torpey, M., Marge, A. Means to improve the thermal conductivity of foam insulation. *J. Cell. Plast.* **1992**, *28*,
773 571–583, doi.org/10.1177/0021955X9202800
- 774 58. Zhao, J., Zhao Q., Wang, L., Wang C., Guo B., Park, C. B., Wang, G.,. Development of high heat insulation and compressive strength
775 BPP foams using mold-opening foam injection molding with in-situ fibrillated PTFE fibers. *Eur. Polym. J.* **2018**, *98*, 1–10,
776 https://doi.org/10.1016/j.eurpolymj.2017.11.001.
- 777 59. Hou, J., Zhao, G., Wang, G., Zhang, L., Dong, G., Li, B., Ultra-high expansion linear polypropylene foams prepared in a semi-molten
778 state under supercritical CO₂. *J. Supercrit. Fluids* **2019**, *145*, 140–150, https://doi.org/10.1016/j.
- 779 60. Yin, D., Mi, J., Zhou, H., Wang, X., Tian, H. Fabrication of branching poly (butylene succinate)/cellulose nanocrystal foams with
780 exceptional heat insulation, *Carbohydr. Polym.* **2020**, *247*,116708–116717, https://doi.org/10.1016/j.
- 781 61. Shi, Z., Zhao, G., Lei Zhang, L., Wang, G., Chai, J., Ultralight and hydrophobic PVDF/PMMA open-cell foams with outstanding heat-
782 insulation and oil-adsorption performances fabricated by CO₂ molten foaming. *Journal of CO₂ Utilization* **2022**, *63*, 102108,
783 doi.org/10.1016/j.jcou.2022.102108.
- 784 62. Sánchez-Calderón, I., Sillero, Á., Lizalde-Arroyo, F., Bernardo, V., Martín-de-León, J., Rodríguez-Pérez, M. J. **2023**. Evaluation of
785 methods to accurately characterize the thermal conductivity of micro-and nanocellular polymers based on poly(methyl-
786 methacrylate) (PMMA) produced at lab-scale. *Polymer Testing* **2023**, *117*, 107842,
787 https://doi.org/10.1016/j.polymertesting.2022.107842.
788
- 789